

# A whole-brain connectivity map of mouse insular cortex

Daniel A. Gehrlach<sup>1,2</sup>, Thomas N. Gaitanos<sup>1</sup>, Alexandra S. Klein<sup>1,2</sup>, Caroline Weiland<sup>1</sup>, Alexandru A. Hennrich<sup>3</sup>, Karl-Klaus Conzelmann<sup>3</sup>, Nadine Gogolla<sup>1\*</sup>

<sup>1</sup>Max Planck Institute of Neurobiology, Circuits for Emotion Research Group, Am Klopferspitz 18, 82152 Martinsried, Germany

<sup>2</sup>International Max-Planck Research School for Molecular Life Sciences, Munich, Germany

<sup>3</sup>Max von Pettenkofer-Institute & Gene Center, Medical Faculty, Ludwig-Maximilians-University Munich, Feodor-Lynen-Strasse 25, 81377 Munich, Germany

\* Corresponding author:

Nadine Gogolla ([ngogolla@neuro.mpg.de](mailto:ngogolla@neuro.mpg.de))

Max Planck Institute of Neurobiology

Am Klopferspitz 18

82152 Munich-Martinsried

Germany

## 1 **Abstract**

2 The insular cortex (IC) plays key roles in emotional and regulatory brain functions and is  
3 affected across psychiatric diseases. However, the brain-wide connections of the mouse IC have  
4 not been comprehensively mapped. Here we traced the whole-brain inputs and outputs of the  
5 mouse IC across its rostro-caudal extent. We employed cell-type specific monosynaptic rabies  
6 virus tracings to characterize afferent connections onto either excitatory or inhibitory IC neurons,  
7 and adeno-associated viral tracings to label excitatory efferent axons. While the connectivity  
8 between the IC and other cortical regions was highly reciprocal, the IC connectivity with  
9 subcortical structures was often unidirectional, revealing prominent top-down and bottom-up  
10 pathways. The posterior and medial IC exhibited resembling connectivity patterns, while the  
11 anterior IC connectivity was distinct, suggesting two major functional compartments. Our results  
12 provide insights into the anatomical architecture of the mouse IC and thus a structural basis to  
13 guide investigations into its complex functions.

## 14 **Introduction**

15 The insular cortex (IC or insula) has been suggested to mediate a wide variety of brain functions,  
16 such as the processing of external and bodily sensory information ([Kurth, Zilles, Fox, Laird, &](#)  
17 [Eickhoff, 2010](#)), bodily- and self-awareness ([Craig, 2009](#); [Craig, 2011](#)), emotion regulation  
18 ([Etkin, Büchel, & Gross, 2015](#)), feelings and complex social-affective functions like empathy  
19 ([Damasio & Carvalho, 2013](#)), and switches between large-scale brain networks ([Menon &](#)  
20 [Uddin, 2010](#)).

21  
22 Rodent studies further demonstrated roles for the IC in multisensory ([Gogolla, Takesian, Feng,](#)  
23 [Fagiolini, & Hensch, 2014](#); [Rodgers, Benison, Klein, & Barth, 2008](#)) and pain processing ([Tan et](#)  
24 [al., 2017](#)), representation of valence ([Wang et al., 2018](#)), learning and memory ([Bermúdez-](#)  
25 [Rattoni, Okuda, Roozendaal, & McGaugh, 2005](#); [Lavi, Jacobson, Rosenblum, & Lüthi, 2018](#)),  
26 social interactions ([Rogers-Carter et al., 2018](#)), gustation ([Peng et al., 2015](#); [Wang et al., 2018](#)),  
27 drug cravings and malaise ([Contreras, Ceric, & Torrealba, 2007](#)), and aversive states such as  
28 hunger, thirst, and anxiety ([Gehrlach et al., 2019](#); [Livneh et al., 2017, 2020](#)).

29 While anatomical studies in diverse species highlight that the insula is one of the most complex  
30 anatomical hubs in the mammalian brain ([Allen, Saper, Hurley, & Cechetto, 1991](#); [Cauda et al.,](#)

31 [2012; David F. Cechetto & Saper, 1987; Menon & Uddin, 2010; Yasui, Breder, Safer, &](#)  
32 [Cechetto, 1991](#)), to date, there is no comprehensive connectivity map of the IC of the mouse, a  
33 genetically accessible model organism widely employed in systems neurosciences.

34 Here, we aimed at providing a comprehensive input and output connectivity description of the  
35 mouse IC to facilitate the mechanistic investigation of insula functions. Furthermore, we  
36 compared the connectivity structure of the IC along its rostro-caudal axis to establish a  
37 connectivity-based compartmentalization that may facilitate the comparison across species.  
38 Indeed, most physiological and functional studies target specific subregions often referred to as  
39 aIC and pIC without clear consensus on borders and coordinates of these regions. Towards the  
40 goal of providing a connectivity-based structure to future functional studies, we divided the  
41 mouse IC into three equally large subdivisions along its rostro-caudal extent, namely an anterior,  
42 medial, and posterior insular part (aIC, mIC, and pIC, respectively) spanning its entire extent.  
43 Although connectivity differences between granular (GI), dysgranular (DI) or agranular (AI)  
44 parts of the IC have been reported previously ([Maffei, Haley, & Fontanini, 2012](#)), we did not  
45 distinguish them here, due to the technical challenge of specifically targeting these layers.  
46 Instead, we focus here on cell-type specific monosynaptic retrograde rabies virus tracings  
47 ([Wickersham, Lyon, et al., 2007](#)) to separately map inputs to excitatory and inhibitory neurons of  
48 the IC across all of its layers. To label outputs, we performed axonal AAV labeling of excitatory  
49 efferents of the aIC, mIC and pIC.

50 We provide a whole-brain analysis of bidirectional connectivity of the longitudinal IC  
51 subdivisions for the two major neuronal subclasses that is excitatory pyramidal neurons and  
52 inhibitory interneurons.

## 53 **Results**

## 54 **Viral tracing approach to reveal the input-output connectivity of the mouse** 55 **IC**

56 To map the connectivity of the entire mouse IC, we injected viral tracers into three evenly spaced  
57 locations along the rostro-caudal axis with the aim of comprehensively tracing from its entire  
58 extent and to assess possible parcellation of the mouse IC into connectivity-based subdomains.  
59 The most anterior region, aIC ranged from +2.45 mm to +1.20 mm from Bregma; the medial  
60 part, mIC, from +1.20 mm to +0.01 mm from Bregma, and the posterior part, pIC, from +0.01  
61 mm to -1.22 mm from Bregma (see also **Fig. 1c**).

62 In order to trace the monosynaptic inputs to the IC we utilized a modified SADΔG-eGFP(EnvA)  
63 rabies virus (RV), which has been shown to label monosynaptic inputs to selected starter cells  
64 with high specificity (Wall, Wickersham, Cetin, De La Parra, & Callaway, 2010; Wickersham,  
65 Finke, Conzelmann, & Callaway, 2007). This virus lacks the genes coding for the rabies virus  
66 glycoprotein (G) and is pseudotyped with the avian viral envelope EnvA. This restricts its  
67 infection to neurons expressing the avian TVA receptor and to monosynaptic retrograde infection  
68 of afferents (**Fig. 1a**). We infected the IC of CamKIIα-Cre and GAD2-Cre expressing mouse  
69 lines to specifically target TVA and rabies virus glycoprotein expression to excitatory pyramidal  
70 or inhibitory interneurons, respectively (see **Fig. 1a** and **Methods**).

71 In order to trace and quantify the axonal projections (outputs) of the IC, we injected Cre-  
72 dependent adeno-associated virus (AAV2/5-DIO-eYFP) into CamKIIα-Cre and GAD2-Cre  
73 transgenic mice (see **Fig 1b** and **Methods**). We did not observe long-range projections from IC  
74 GAD2-Cre tracings (data not shown). Therefore, we here only present outputs from excitatory  
75 projection neurons performed in CamKIIα-Cre transgenic mice.

76 We first assessed the spread and quality of our starter cell populations for both AAV and RV  
77 tracings in a semi-automated manner (**Fig. 1c, Suppl. Fig. 1a, b** and **Methods**). For RV  
78 experiments, starter cells were counted when double positive for eGFP (i.e. RV<sup>+</sup>) and mCherry  
79 (i.e. TVA<sup>+</sup>). For AAV tracings, starter cells were counted as eYFP-positive cell bodies. We  
80 thereby defined both the total number and location of all starter cells. The bulk of the starter  
81 populations for the distinct IC subdivisions were highly separated and non-overlapping for both  
82 RV and AAV tracings (**Fig. 1c, Suppl. Fig. 1c**). In some cases, a very small percentage of starter  
83 neurons were detected in regions outside the boundaries of the IC, including in the Pir, S1 and

84 S2, as well as the M1. In these cases we asked if these contaminations affected the qualitative  
85 connectivity structure by comparing them to tracings without contamination. If not, they were  
86 included in this study.

87 To compile the whole-brain connectivity maps for both RV and AAV tracings, we cut coronal  
88 sections (ranging from +2.65 to -6.2 mm relative to Bregma) and analyzed the long range,  
89 ipsilateral connectivity on sections approximately 140  $\mu\text{m}$  apart (**Suppl. Fig. 2a, b, Methods**).  
90 For the rabies virus tracings, we obtained brain-wide inputs ranging from 5000-45000 cells, with  
91 convergence ratios ranging from 6-15 (**Suppl. Fig. 1c**). We accounted for the variability between  
92 tracings by normalizing cell counts per region of interest (ROI) to the total number of neurons  
93 per brain. We additionally obtained the cell density of each ROI as cells/ $\text{mm}^2$ .

94 For the AAV tracings, we identified a total of 600 - 800 million pixels per brain as IC efferents  
95 (**Suppl. Fig. 1c**). To account for animal-to-animal variation, we normalized each ROI to the total  
96 amount of pixels identified brain-wide. Additionally, we calculated the innervation density, given  
97 in percent of maximal ROI pixel count.

98 For both RV and AAV tracings, we determined the spatial location of the starter neurons. Within  
99 this immediate surround of the starter cells we did not quantify inputs or outputs due to the  
100 ambiguity to distinguish starter cells from input or outputs, respectively (**Fig. 1c, Suppl. Fig. 2c**).  
101 Thus the quantifications of this study focus on the long-range connectivity of IC subdivisions.

102 To ensure Cre-dependence of our approach, we performed control infections of WT mouse  
103 brains. Mice lacking Cre-recombinase should not express eGFP when infected with RV. Indeed  
104 only some GFP+ neurons were detected at the injection sites within the boundaries that we  
105 would normally exclude from our quantitative analysis (**Suppl. Fig. 2c**). To test the dependence  
106 on RG supplementation for the synaptic jump of the virus and thus to ensure the monosynaptic  
107 restriction, we injected TVA and RV into CamKII $\alpha$  or GAD2-Cre mice without the addition of  
108 RG. As expected, eGFP expression was detected in transfected neurons, but none was expressed  
109 outside the boundaries that we would normally exclude from our quantitative analysis, indicating  
110 that no synaptic jump had occurred and no long-range projections were labelled (**Suppl. Fig. 2c**).

## a RV tracing strategy

*CamKII $\alpha$ -Cre* or *Gad2-Cre*

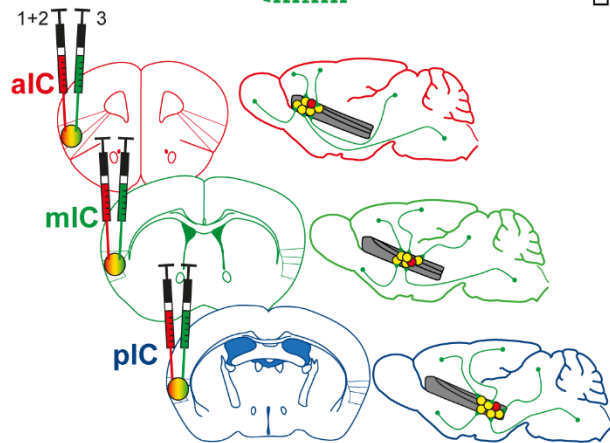
1) AAV2/8-FLEX-TVA-mCherry



2) AAV2/8-FLEX-RG



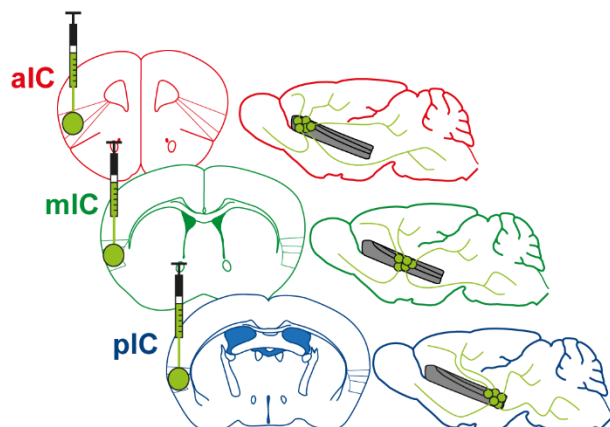
3) RV-SAD $\Delta$ G-eGFP(EnvA)  $\downarrow$  3 weeks



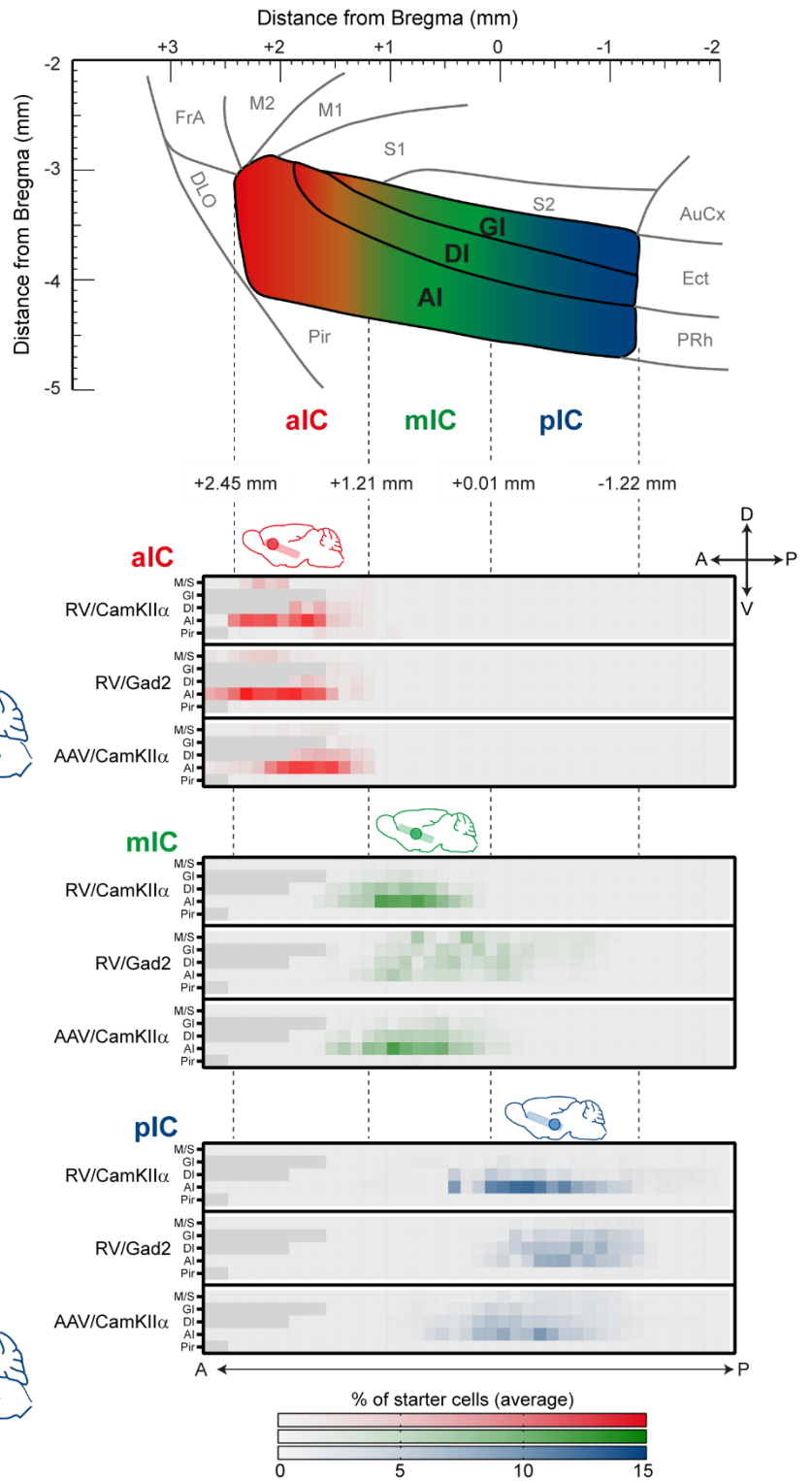
## b AAV tracing strategy

*CamKII $\alpha$ -Cre*

AAV2/5-DIO-eYFP



## c Distribution of starter populations



111 **Figure 1. Tracing strategy and localizations for input and output viral tracings from distinct IC**  
112 **subregions.**

113 Schematic representation of Cre-dependent **(a)** monosynaptic retrograde Rabies virus tracing (RV), and  
114 **(b)** anterograde axonal AAV tracings (AAV) used to determine respective input and output connectivity to  
115 the IC. Tracings were performed in both excitatory (*CamkIIa*-Cre) and inhibitory (*Gad2*-Cre) mouse lines  
116 for RV, and only in the *CamkIIa*-Cre mouse line for AAV. For RV tracings, AAV-FLEX helper viruses  
117 expressing mCherry-tagged TVA (1) and rabies-virus-specific G protein (2) were co-injected into the IC  
118 region of interest. Three weeks later EnvA-coated, eGFP-expressing modified RV lacking G protein was  
119 injected at the same location (3). For anterograde tracings, a one-off injection of eYFP-expressing AAV-  
120 FLEX virus was administered into the chosen location. Three distinct IC subdivisions were chosen for  
121 each tracing technique: anterior (aIC, red), medial (mIC, green) or posterior (pIC, blue). **(c)** Schematic  
122 illustration of the lateral view of the IC including distances from Bregma (top panel) and heatmap showing  
123 average starter cell distribution for each tracing strategy at each specific IC target (bottom panels). The  
124 three IC target subdivisions were mostly non-overlapping, and only a minimal percentage of cells were  
125 detected in the Motor and Sensory Cortex (M/S), or Piriform Cortex (Pir) neighboring the IC. n = 3 mice per  
126 injection site/tracing strategy. Heatmap intensity scale is the same for all three IC target subdivisions.  
127 Regions absent at specific Bregma levels indicated by dark gray squares.

128 **Whole brain input/output map of mouse IC**

129 To provide a detailed account of the brain-wide connectivity of the mouse IC, we analyzed its  
130 reciprocal connectivity with 75 anatomical subregions (the detailed connectivity maps of the IC  
131 with all subregions analyzed can be found in the **Suppl. Fig. 3-5**). To first gain an overview of  
132 the overall IC connectivity, we pooled these detailed datasets into overall connectivity patterns  
133 between the IC and 17 larger brain regions (**Figure 2**).

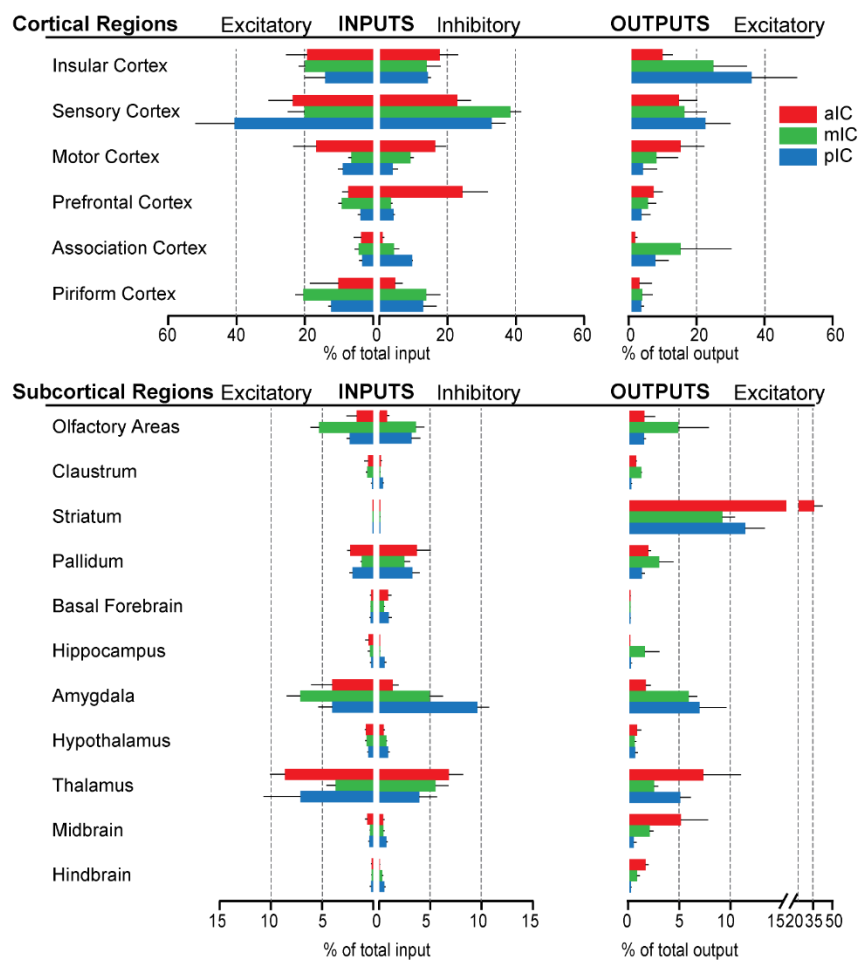
134 Overall, although there were marked quantitative differences, the anterior to posterior extent of  
135 the IC connected to the same major brain regions and no large brain region was exclusively  
136 connected to one but not the other IC regions. Furthermore, we did not observe any marked  
137 differences in the connectivity patterns of inhibitory versus excitatory neurons, instead both  
138 major neuronal cell classes exhibited qualitatively similar connectivity patterns. Overall, all IC  
139 subdivisions received strong sensory inputs from primary and secondary sensory cortical regions,  
140 with an especially strong drive onto pIC excitatory neurons. Connectivity from prefrontal cortex  
141 regions was especially marked to the inhibitory neurons of the aIC. Furthermore, we found heavy  
142 intra-insular connections. Especially the pIC and mIC sent strong projections to the other IC  
143 subdivisions, while the projection strength of the aIC was smaller, suggesting stronger  
144 feedforward projections from posterior to anterior parts of the IC.

145 Concerning the connectivity with subcortical brain regions, overall the IC connectivity was  
146 characterized by three major connections: strong projections to the striatum, and reciprocal  
147 connections with diverse subregions of the amygdala and the thalamus.

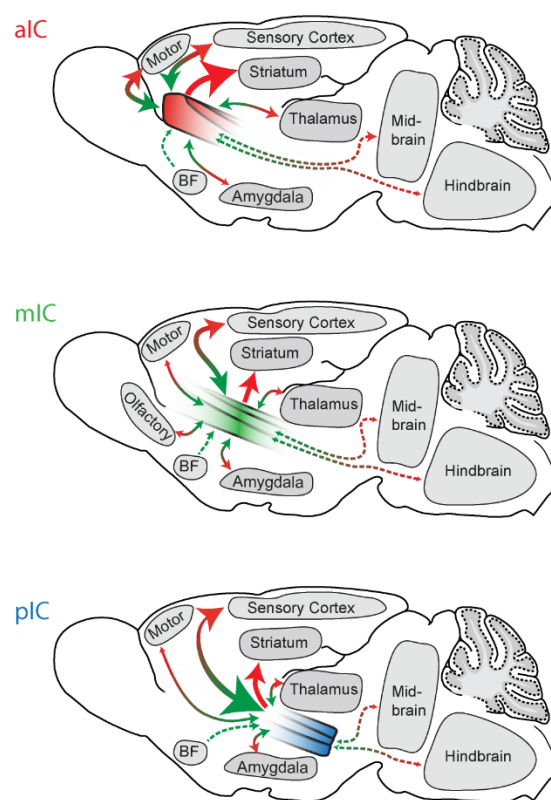
148 Focusing our analyses on the quantitative differences between IC subdivisions along the rostro-  
149 caudal axis, we found that, overall, the pIC received twice as many inputs from the sensory  
150 cortices ( $41 \pm 11\%$  of total excitatory input connectivity) as the other IC subdivisions ( $20 \pm 5\%$   
151 and  $23 \pm 7\%$  for mIC and aIC, respectively). In contrast, the aIC received the majority of inputs  
152 from the motor cortex.

153 The aIC sent almost one third of its projections to the striatum, while for the mIC and pIC about  
154 10% of the efferents were innervating the striatum. (aIC  $32 \pm 6\%$  of outputs, as compared to  $9 \pm$   
155  $1\%$  for mIC and  $11 \pm 2\%$  for the pIC). An inverse pattern was observed for the amygdala  
156 projections. About 5-7 % of the mIC's and pIC's efferents were directed to different amygdala  
157 subnuclei, while only 1.5 % of the aIC efferents were directed to the amygdaloid complex.  
158 Interestingly, the mIC, containing the 'gustatory cortex' was most heavily connected with  
159 olfactory regions and much more so than pIC or aIC. Given the strong connectivity of the entire  
160 IC with important subcortical regions, such as the striatum, the amygdala or the thalamus, we  
161 aimed at describing the IC connectivity to these major interactions partners in more detail in the  
162 following sections.

## a Whole-brain IC connectivity to 17 major brain regions



## b Input/output maps for broad IC subdivisions



### 163 **Figure 2. Whole-brain IC connectivity map.**

164 **(a)** Comparison of inputs to excitatory and inhibitory IC neurons (left) and outputs of excitatory neurons of  
 165 the IC (right) of all three IC subdivisions (aIC, red; mIC, green; pIC, blue) across the 17 major brain regions  
 166 that displayed connectivity. Region values are given as percentage of total cells (RV) or of total pixels  
 167 (AAV). Data is shown as average  $\pm$  SEM.  $n = 3$  mice per condition. Top panel shows cortical connectivity,  
 168 bottom panel shows subcortical connectivity. **(b)** Individual input-output maps for the three IC subdivisions  
 169 highlighting selected brain regions. Weight of arrowhead and thickness of arrow shaft indicate strength of  
 170 connection. Green arrowheads indicate inputs, red arrowheads indicate outputs.

## 171 **IC-amygdala connectivity**

172 It has been well established that IC and amygdala are heavily interconnected (Allen et al., 1991;  
173 Augustine, 1996; McDonald, Shammah-Lagnado, Shi, & Davis, 1999; Santiago & Shammah-  
174 Lagnado, 2005) and many important brain functions, for example in valence processing or  
175 emotion regulation and awareness, have been suggested to rely on this anatomical link. However,  
176 we still lack a detailed understanding of the functional interplay of IC and amygdala, a network  
177 affected across many psychiatric disorders. Recent studies in mice have begun to expose  
178 functionally distinct projection pathways between the IC and amygdala (Gehrlach et al., 2019;  
179 Lavi et al., 2018; Schiff et al., 2018; Wang et al., 2018). We thus next analyzed the detailed  
180 connectivity between the nuclei of the mouse amygdala and the IC.

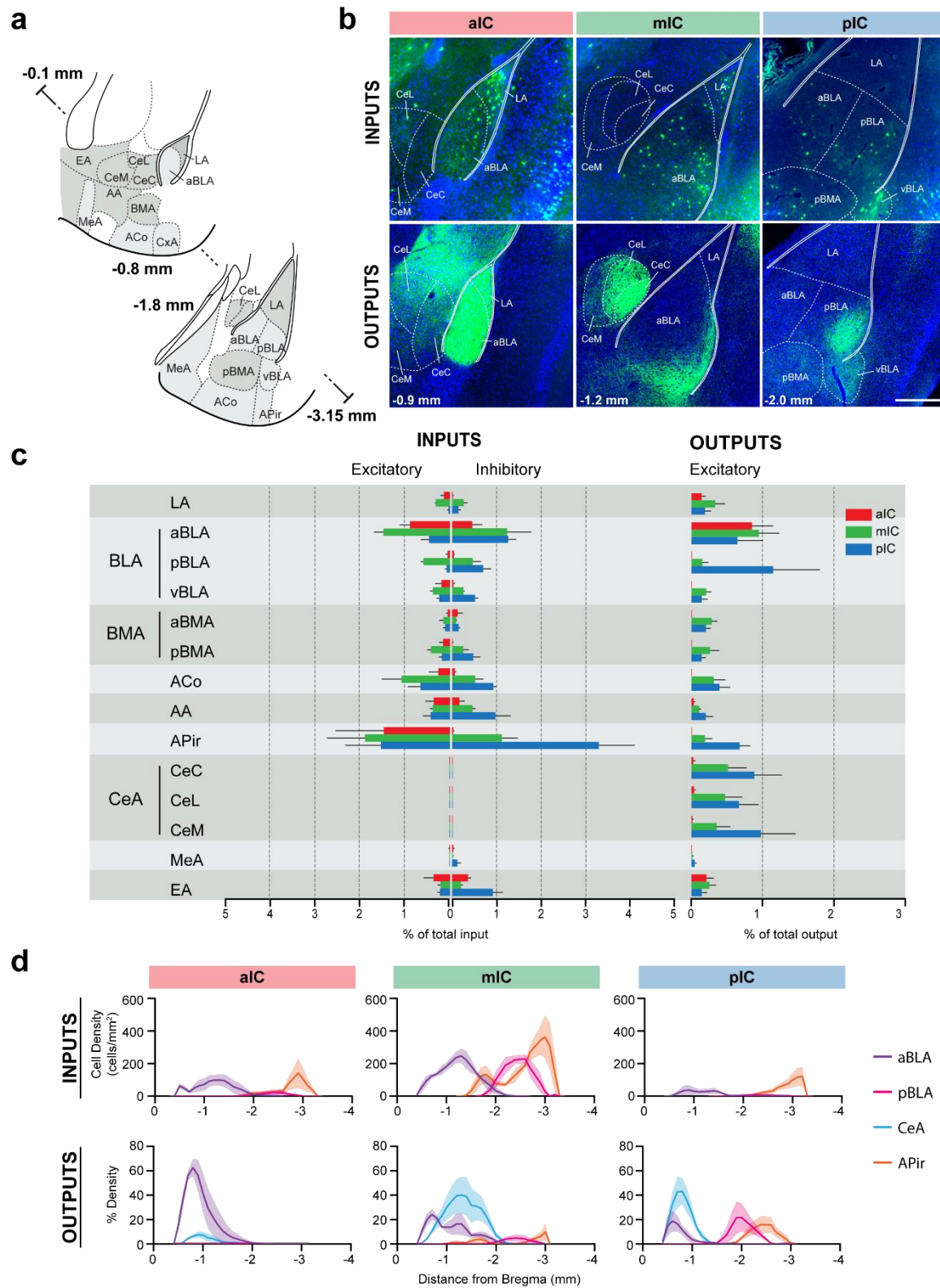
181 As expected, the afferent connectivity from the amygdala to all three IC subdivisions was  
182 provided by cortex-like subregions of the amygdala, including the basolateral amygdala (BLA)  
183 and amygdalopiriform transition area (APir), and not from striatum-like nuclei such as the  
184 central nucleus of the amygdala (CeA) and medial amygdaloid nucleus (MeA) (**Fig. 3a-c**).

185 Interestingly, the APir was one of the rare brain regions which sent differently strong inputs to  
186 excitatory versus inhibitor neurons of the IC. This difference was most pronounced in the aIC  
187 where inhibitory neurons received very little inputs from the APir as compared to the excitatory  
188 neurons (0.07% vs 1.5 %).

189 Additionally, when comparing inputs from APir to inhibitory neurons of aIC with those of mIC  
190 and pIC, a clear difference emerged, with the inhibitory neurons of pIC receiving most inputs  
191 (>3% connectivity in the pIC). Interestingly, when comparing afferents from the amygdala to  
192 excitatory neurons of aIC, mIC and pIC, only small differences were found, with the mIC being  
193 slightly more innervated.

194 Output projections from the IC, on the other hand, innervated all amygdala regions except the  
195 MeA (**Fig. 3c**). There were two opposing gradients along the rostro-caudal axis of the IC  
196 depending on the amygdala nuclei target. For example, we found a bias of pIC innervating CeA,  
197 APir and the posterior part of the BLA (pBLA). On the other hand, the anterior part of the BLA  
198 (aBLA) was more densely innervated by the aIC in comparison to mIC or pIC (Wang et al.,  
199 2018). Interestingly, the aIC did not connect with more posterior basolateral regions of the  
200 amygdala, such as the pBLA, a pattern clearly visible in the density profile (**Fig. 3d**, bottom left

201 panel). In addition, the aIC did not innervate any other nucleus of the amygdala aside from a  
202 sparse projection to the extended amygdala (EA).



### 203 **Figure 3. IC-amygdala connectivity**

204 **(a)** Coronal sections depicting the amygdala with its subregions. Distances are provided as anterior-  
205 posterior positions relative to Bregma. **(b)** Representative images from excitatory inputs (top row, eGFP-  
206 expressing neurons) and outputs (bottom row, eYFP-positive neurons). Different Bregma levels are shown  
207 for each IC target site, as indicated on the images (-0.9 mm, -1.2 mm, -2.0mm). Scale bar = 200  $\mu$ m. **(c)**  
208 Comparison of excitatory and inhibitory inputs detected in the amygdala (left) and excitatory outputs from  
209 the IC to the amygdala (right) in percent of total in- or output, respectively (aIC, red; mIC, green; pIC, blue).  
210 Data is shown as average  $\pm$  SEM. n = 3 mice per condition. **(d)** Input cell density (top row) and percent  
211 output density (bottom row) plots along the anterior-posterior axis covering the entire amygdala. We  
212 selected aBLA, pBLA, CeA and APir to provide the areas with most differences between the IC subdivisions.  
213 n = 3 mice per condition. Data shown as average  $\pm$  SEM.

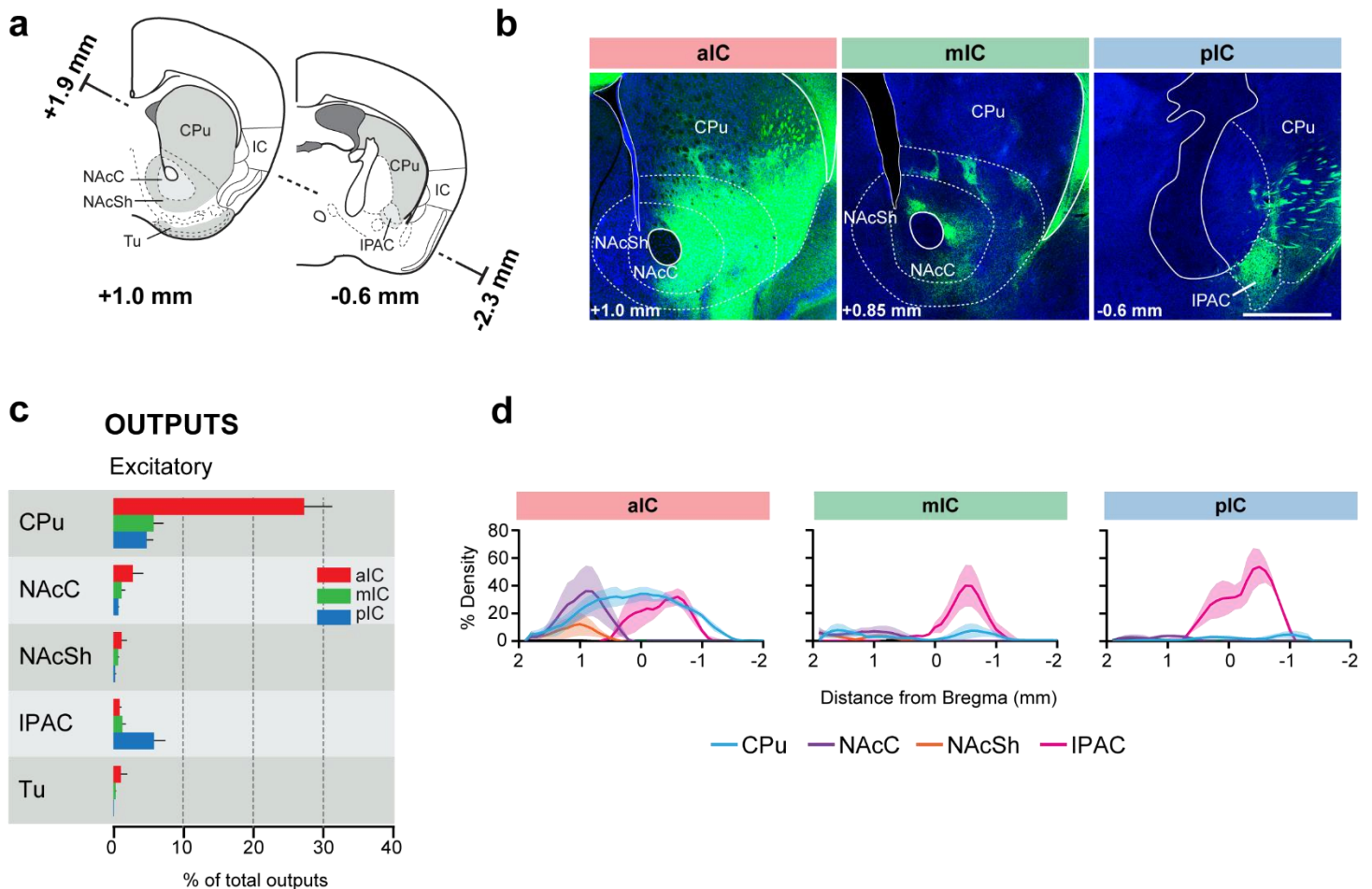
### 214 **IC-striatum connectivity**

215 The striatum, the main input region of the basal ganglia, is implicated in optimizing behavior  
216 through refining action selection, reward- and aversion processing, habit formation and  
217 modulating motor responses ([Graybiel & Grafton, 2015](#)). Previous work in rodents describing  
218 projections to the striatum indicated that the IC targeted the ventral and ventro-lateral striatum,  
219 converging with projections from piriform cortex (Pir), medial prefrontal cortex (mPFC),  
220 perirhinal cortex (PERI) and the BLA ([Hintiryan et al., 2016](#); [Hunnicutt et al., 2016](#)).

221 We analyzed the detailed connectivity between the IC and the striatum (**Fig 4**), focusing on the  
222 IC-to-striatum outputs, given that there was, as expected, no afferent connection from the  
223 striatum to any IC subdivision (**Fig 2a**). Consistent with a previous study ([Hunnicutt et al.,](#)  
224 [2016](#)), we found that the ventral regions of the striatum were more innervated by IC projections  
225 than dorsal regions (**Fig 4b**). However, the vast majority of the innervations we detected came  
226 specifically from the aIC, which displayed both broad and very dense projections across the  
227 ventro-lateral caudate putamen (CPu), spanning almost the entire structure along its rostro-caudal  
228 axis (**Fig 4b-d**). Furthermore, the nucleus accumbens core (NAcC) and the interstitial nucleus of  
229 the posterior limb of the anterior commissure (IPAC) were densely innervated by aIC  
230 projections, despite their low relative percentage of outputs (**Fig. 4b-d**).

231 The mIC and pIC also projected the CPu, but to a much weaker extent than aIC (approximately  
232 5-fold lower). However, both mIC and pIC densely innervated the IPAC (to around 60% density)  
233 (**Fig. 4d**). Overall, mIC and pIC showed a very similar connectivity pattern to the striatum with  
234 9% and 11% of total output, respectively. In contrast, aIC output to the striatum represents the

235 largest output out of all regions innervated by aIC (31.8%). Both, mIC and pIC specifically  
 236 innervated striatal patches (Brimblecombe & Cragg, 2017), as seen for mIC in Fig. 4b.  
 237 Taken together, we found a large difference in the innervation of the striatum along the rostro-  
 238 caudal axis of the insula, with the aIC providing the strongest projections.



239 **Figure 4. IC-striatum connectivity**

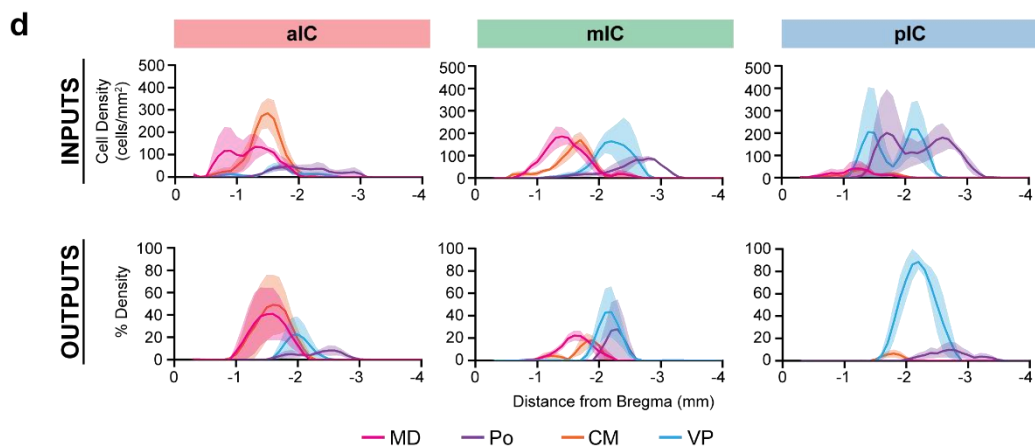
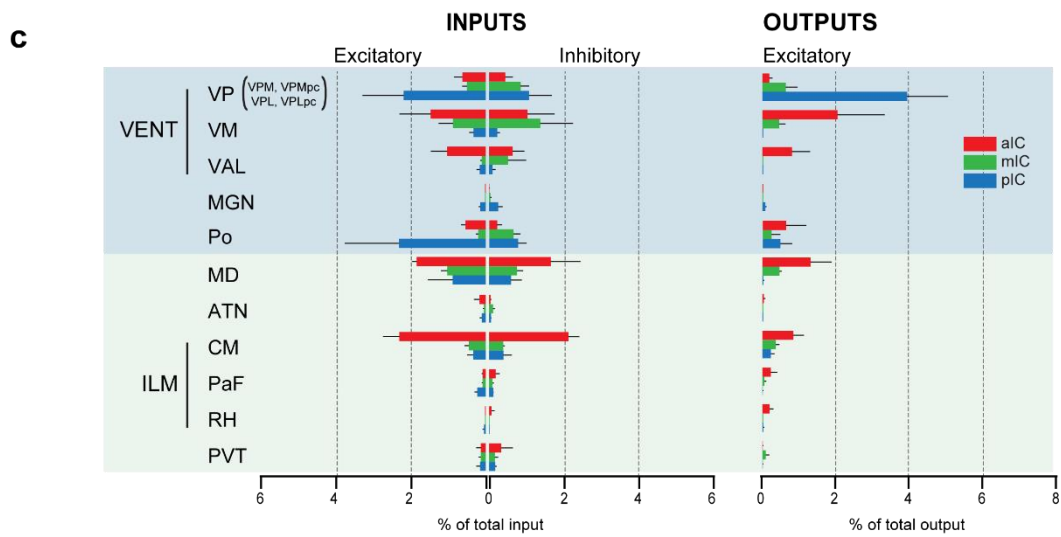
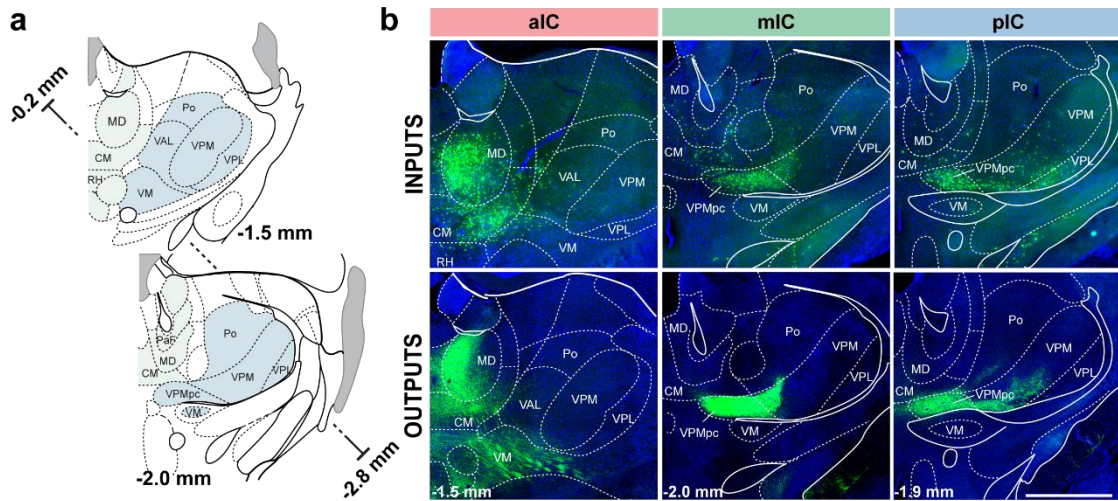
240 **(a)** Coronal sections depicting the striatum with its subregions. **(b)** Representative images from excitatory  
 241 outputs (eYFP-positive neurons). Note the dense innervation of CPu, NAcC and NAcSh by the aIC.  
 242 Different Bregma levels are shown for each aIC, mIC and pIC, as indicated on the images. Scale bar = 500  
 243  $\mu$ m. **(c)** Comparison of excitatory outputs from the three IC subdivisions to the striatum in percent of total  
 244 output (aIC, red; mIC, green; pIC, blue). Values are given as percentage of total pixels. Data shown as  
 245 average  $\pm$  SEM, n = 3 mice per condition. **(d)** Plots depict the density of IC innervation along the anterior-  
 246 posterior axis of the striatum. n = 3 mice per condition, data shown as average  $\pm$  SEM.

## 247 **IC-thalamic connectivity**

248 We next assessed the third largest subcortical connectivity partner of the IC: the thalamus.  
249 Thalamo-cortical projections are thought to be essential drivers of cortical activity in sensory  
250 areas and associative brain regions (Hunnicutt et al., 2014). Cortico-thalamic feedback  
251 projections stemming from layer 6, in turn, shape thalamic cell activity via monosynaptic and  
252 disynaptic connections (Crandall, Cruikshank, & Connors, 2015). The function of cortical  
253 regions has often been inferred by characterizing the type of thalamic input they receive  
254 (Sherman & Guillery, 2006).

255 The afferent connectivity to the aIC originated mainly from higher-order associative and motor  
256 nuclei, with the majority of inputs arising from the polymodal association group of thalamic  
257 nuclei (medio-dorsal (MD) and centro-median (CM) nuclei). Furthermore, the aIC received  
258 innervation from two sensory-motor related nuclei, the ventro-medial (VM) and the ventral  
259 antero-lateral (VAL) nucleus. The afferents of pIC, on the other hand, were majorly originating  
260 from sensory-related nuclei, with the greatest inputs originating in the posterior complex (Po)  
261 and the ventral posterior complex (VPC). While the pIC also received inputs from the MD  
262 (though less than the aIC), it was only weakly innervated by the CM. Interestingly, the afferents  
263 of mIC exhibited characteristics of both aIC and pIC, receiving projections from sensory-, motor-  
264 related, and higher-order thalamic nuclei.

265 As expected from thalamo-cortical pathways (Hunnicutt et al., 2014), IC outputs reciprocated  
266 their thalamic inputs. For example, the aIC strongly and densely innervated the VM, MD and  
267 CM, thus putatively closing the thalamo-cortico-thalamic loop. The pIC strongly and densely  
268 innervated the VPC in particular, and had almost no projections to any other thalamic nuclei.



269 **Figure 5. IC-thalamus connectivity**

270 **(a)** Coronal sections depicting the thalamus with Subregions that connect to the IC. **(b)** Representative  
271 images from excitatory inputs (top row, eGFP-expressing cell bodies) and outputs (bottom row, eYFP-  
272 positive neurons). Different Bregma levels are shown for each IC subdivision as indicated on the images.  
273 Scale bar = 500  $\mu\text{m}$ . **(c)** Comparison of inputs to excitatory or inhibitory neurons of all three IC subdivisions  
274 (left) and of outputs from excitatory IC neurons to the thalamus (aIC, red; mIC, green; pIC, blue). Values  
275 are calculated as percentage of total cells (RV) or of total pixels (AAV). Data shown as average  $\pm$  SEM, n  
276 = 3 mice per condition. **(d)** Input cell density (top row) and output density (bottom row) plots along the  
277 anterior-posterior axis. Thalamus regions of interest are shown, n = 3 mice per condition, data shown as  
278 average  $\pm$  SEM.

279 **Reciprocal connectivity**

280 We next investigated the reciprocity of the IC connectivity with other brain areas by correlating  
281 inputs to excitatory neurons with their respective outputs (**Fig. 6a**).

282 We first assessed the reciprocity of the connections between the IC and other cortical regions.

283 We found a significant correlation for the connectivity of the mIC and pIC with other cortical  
284 regions and a strong trend for correlation for the mIC with other cortical regions. Thus, the IC  
285 was mostly bidirectionally connected to many other cortical regions.

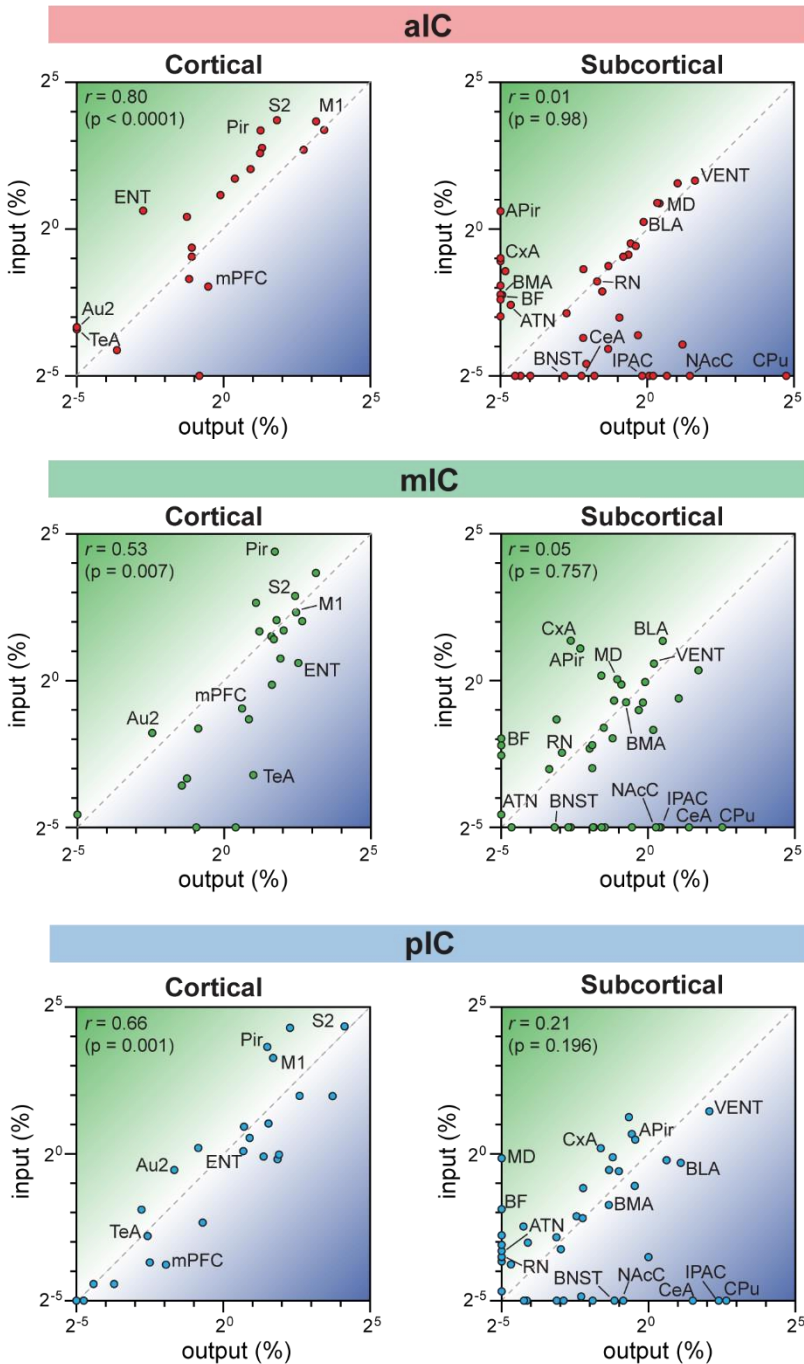
286 Subcortical regions, on the other hand, were most often not reciprocally connected to the IC.

287 Instead, we could define many subcortical IC connections as either being input-dominated  
288 (bottom-up connectivity) or output-dominated (top-down) (**Fig. 6b**). No region strongly reversed  
289 its top-down or bottom-up characteristic when comparing between aIC, mIC and pIC. However,  
290 the mid- and hindbrain nuclei received less pIC innervation compared to aIC and mIC (e.g.,  
291 compare raphe nuclei (RN) input vs output coordinates in **Fig. 6a**), suggesting that pIC has a less  
292 direct influence on neuromodulatory systems.

293 Overall, the thalamic and amygdala nuclei tended to be more bottom-up influenced, further  
294 supporting the role for the IC in processing multi-sensory and emotion-related signals ([Simmons  
295 et al., 2013](#)); whereas the striatum, midbrain and hindbrain connectivity was mostly top-down,  
296 supporting a direct role of the IC in modulating ongoing behavioral responses.

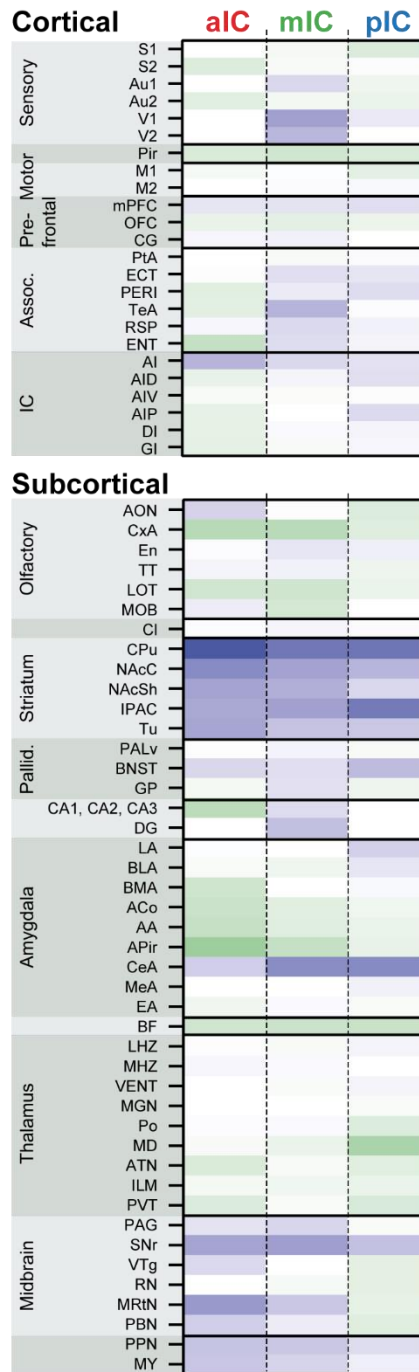
**a**

**Input/output correlations**



**b**

**Bottom-up Reciprocal Top-down**  
 15 -15  
 ( $\log_2$ )



## 297 **Figure 6. IC input-output relationships**

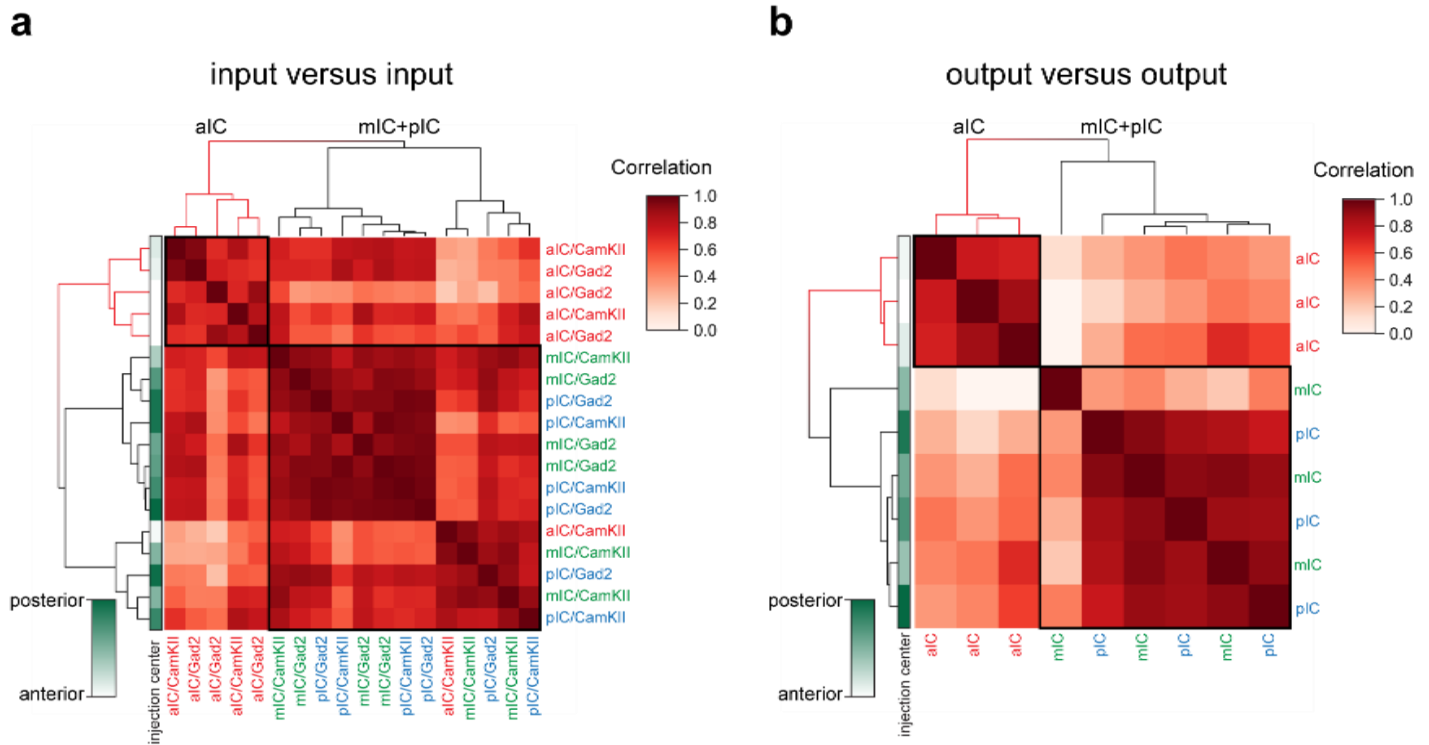
298 The global dataset was further subdivided into subregions of higher specificity (see **Suppl. Fig.S3-5**). **(a)**  
299 The average value for each excitatory input and output was correlated for the three IC subdivisions. Data  
300 is divided into cortical (left panels) and subcortical (right panels) regions. Subregions that lacked both input  
301 and output neurons are not included in the graphs. Note the high correlation in the cortical connectivity as  
302 compared to the connectivity in the subcortex for all datasets ( $r$  = Pearson's correlation coefficients). **(b)**  
303 Heatmaps showing fold-difference between inputs to outputs per brain subregion for each IC target. Green  
304 gradient represents bottom-up connectivity (inputs>outputs), blue gradient represents top-down  
305 connectivity (inputs<outputs). Subregions where no signal was detected for both input and output conditions  
306 were omitted. Data shown as ratio from the average of 3 mice per condition per IC subdivision. The meaning  
307 of the abbreviations can be found in **Suppl. Table 2**.

## 308 **Comparison of input and output distributions**

309 Throughout our analyses, we have seen distinctions arising between the three IC subdivisions we  
310 targeted. To test whether these observations represent meaningful differences, we correlated in an  
311 unbiased manner all input tracings to each other (including inhibitory and excitatory connectivity  
312 experiments). We additionally performed the same analysis for all output tracings. We compared  
313 the 17 major brain regions in a pairwise fashion and hierarchically clustered the correlation  
314 coefficients (**Fig. 7a,b** and **Methods**). Overall, there was a high degree of similarity for the  
315 input-input comparisons (average correlation coefficients of  $0.7 \pm 0.16$ ), and, to a lesser extent,  
316 for the output-output comparison (average correlation coefficients of  $0.45 \pm 0.28$ ). However, for  
317 both inputs and outputs, two distinct clusters did form, separating the aIC tracings from a  
318 grouped mIC/pIC pool. Furthermore, for both inputs and output correlations (**Fig. 7a and b**), the  
319 mIC and pIC tracings were so similar that they did not fall into separate clusters. Indeed, the  
320 relative location of the starter cell population (left columns, green gradient) did not lead to a  
321 separate clustering of mIC and pIC targeted tracings. Finally, for the input data, there was no  
322 correlation separating excitatory and inhibitory tracings, supporting our conclusions stated earlier  
323 that the IC afferents for these two cell types is similar.

324 Taken together, the input- and output-patterns of aIC suggest a functional difference compared to  
325 mIC and pIC regions. In particular, for the output network, a key difference arises from the high  
326 degree of efferent connectivity between the aIC and striatum, and to a lesser extent, the motor  
327 cortex, as compared with the mIC and pIC (**Fig. 2a**). For inputs to the IC, the difference is not so  
328 profound, with subtle variations in regions such as the motor cortex (as with outputs, biased

329 towards the aIC) the sensory cortex (pIC-biased), the amygdala (slight pIC/mIC bias) and  
330 producing the two clusters.



331 **Figure 7. Connectivity-based subdivisions of the IC**

332 Matrices of hierarchically clustered pair-wise correlation coefficients (Pearson's) of animals (a) inputs vs.  
333 inputs (N = 18 mice) or (b) outputs vs outputs (N = 9 mice). The pair-wise correlations were performed on  
334 the data organized into 17 major brain regions (see Fig 2). Far left gradient bar (green hues) indicates the  
335 center of the starter cells, ranked relative to every mouse in the dataset. Note for both input and output  
336 correlations, a clear cluster forms from the aIC-targeted animals (top left boxed sections and red-colored  
337 dendrograms), whereas the mIC- and pIC-targeted animals intermingle in a second cluster (larger boxed  
338 areas). Interestingly, the clustering algorithm did not separate excitatory (*CamKII $\alpha$* ) from inhibitory (*Gad2*)  
339 rabies virus tracings.

## 340 **Discussion**

341 In this study we systematically mapped the brain-wide input- and output connectivity of  
342 inhibitory and excitatory neurons of three subdivisions of the mouse insular cortex. All IC  
343 subdivisions exhibit multifaceted and brain-wide connectivity patterns, with a substantial degree  
344 of intra-insular cross talk. These factors result in a series of complex, multi-modal hubs,  
345 suggesting that each subdivision is not limited to a single specialized function.

346 By performing unbiased cluster analysis, we found differences in IC connectivity along the  
347 rostral-caudal axis, in particular in regards to both in- and outputs to and from the aIC as  
348 compared to those of the mIC and pIC. For the outputs, this difference is in part due to a  
349 specifically strong ventro-lateral striatum innervation by the aIC. Overall, the aIC also showed a  
350 bias towards connectivity with locomotion-related areas, such as the motor cortices (M1, and  
351 M2), the ventro-medial (VM) and centro-median thalamic (CM) nuclei and, the substantia nigra  
352 and the midbrain reticular nucleus. This connectivity pattern may provide an anatomical  
353 foundation for why optogenetic stimulation of the aIC can elicit appetitive and seeking behavior  
354 and has been described as a ‘positive valence’ region ([Peng et al., 2015](#); [Wang et al., 2018](#)).

355 Overall, our data suggest a general role of the aIC with functional roles beyond that of a “sweet  
356 cortical field” ([Peng et al., 2015](#)), since intra-insular projections from the mIC and pIC, which  
357 process diverse bodily information, are one of its main input sources. Based on its connectivity  
358 and knowledge gained in previous functional studies, the aIC could serve as an integrator of  
359 positive-valence signals that then guide motivated behavior through its downstream projections,  
360 in particular via the ventral striatum and motor cortex. Given our approach we could not dissect  
361 further differences between the dorsal (AID) and ventral division of aIC (AIV), but studies  
362 performed in hamsters and rats have suggested a further distinction of projection patterns  
363 between the AID and AIV ([Hintiryan et al., 2016](#); [Maffei et al., 2012](#); [McDonald et al., 1999](#);  
364 [Reep & Winans, 1982](#)).

365 Interestingly, our correlation and clustering analysis suggests that the mIC is more similar to the  
366 pIC. The GI/DI of the mIC is referred to as the “gustatory cortex” in the Allen Mouse Brain Atlas  
367 ([Lein et al., 2007](#)). Notably, we found that the mIC received strong olfactory related inputs (from  
368 the Pir, APir, and piriform-amygdalar area (CxA)). Furthermore, comparative to either the aIC  
369 and pIC, the mIC sends more outputs to memory related areas, such as the entorhinal cortex and

370 the ventral hippocampus. Indeed, previous studies demonstrated the role of the mIC in  
371 conditioned taste aversion (CTA) (Lavi et al., 2018). Taken together with previous functional  
372 studies, our anatomical description supports a role for the mIC as a learning hub, involved in  
373 various aspects of consummatory behaviors, such as texture processing of food, palatability, taste  
374 aversion or preference. Potentially, this could extend past consummatory domains, into social  
375 transmission of food preferences or reproductive behavior.

376 We also extended our recent findings of pIC connectivity (Gehrlach et al., 2019), and can now  
377 clearly establish it as an anatomically defined subregion of the mouse IC through direct  
378 comparison of its connectivity as compared to the aIC, in particular. The pIC shows a  
379 multimodal convergence of inputs from bodily and limbic information streams with top-down  
380 projections to regions implicated in emotional and motivated functions. This includes innervation  
381 from sensory, autonomic, motor associative and limbic structures. Furthermore, there are more  
382 intra-insular outputs from the pIC than from the aIC, implying a caudal-to-rostral flow of  
383 information, as has been suggested previously (Craig, 2009; Fujita, Adachi, Koshikawa, &  
384 Kobayashi, 2010).

385 Our analysis of the reciprocity of IC connectivity with other cortical or subcortical regions  
386 revealed strong correlations between in- and outputs for cortical regions across all IC subregions.  
387 In contrast, many subcortical regions were connected to IC with a strong bottom-up (RN, basal  
388 forebrain (BF), olfactory regions, and thalamic nuclei) or top-down (CeA, striatum, SNr, and  
389 BNST) bias. These comparisons come with the caveat that we have no physiological  
390 measurements of relative connectivity strength.

391 Interestingly, inhibitory interneurons, irrespective of which IC subdivision was analyzed (APir  
392 aside), displayed very similar connectivity patterns and strength when compared to excitatory  
393 pyramidal neurons. This was supported by our correlation and hierarchical cluster analysis and is  
394 in agreement with several rabies virus tracings studies in other brain regions (Beier et al., 2015;  
395 Do et al., 2016; Luo et al., 2019; Wall et al., 2016) and may underlie the balance of excitation  
396 and inhibition in cortex (Sohal & Rubenstein, 2019; Yizhar et al., 2011).

397 Although this investigation sought to systematically compare brain-wide IC connectivity, there  
398 are limitations that need to be considered. First, despite there being good separation between the  
399 bulk of the starter cell populations into our defined zones, there is a small proportion of overlap

400 that may influence the connectivity. This only affects the results when comparing with mIC  
401 results, as aIC and pIC starter populations were completely separated. Contamination into non-IC  
402 regions may also influence the results we observed, however, we did not find a correlation  
403 between the amount of non-IC starter cells in a specific brain region and an increase in  
404 connectivity to its known targets (data not shown). Displaying data as percentage of total comes  
405 with the caveat that smaller regions are underrepresented, for example the DRN that only  
406 provided below 0.1% of the total inputs consistently projected to the IC. Thus functional  
407 implications cannot solely be determined from the relative number of inputs. The alternative,  
408 using density analysis, underrepresents larger areas, such as the cortical regions (please refer to  
409 the pivot table in the **Suppl. Table 1** which allows custom plots of densities for all data presented  
410 here). Finally, counting labelled fiber presence after AAV infection to detect the output strength  
411 does not directly represent synaptic connectivity. Recent technology using a fluorescent protein  
412 tagged to a synaptic marker (e.g. AAV-DIO-mRuby-T2A-synaptophysin-eGFP, (Knowland et al.,  
413 2017)) or the trans-synaptic infection of AAV1-Cre (Zingg et al., 2017) would overcome this  
414 limitation.

415 Bearing this in mind, this study highlights specific IC connectivity patterns that warrant further  
416 functional investigation. These include the localized targeting of pIC projections to the IPAC,  
417 which may be involved in motivated behaviors like approach, seeking and feeding. In the  
418 amygdala, all IC regions project to the BLA, but only the pIC innervated the pBLA.  
419 Understanding the role of this pathway would help in both describing IC function and the  
420 specificity of amygdala subregions. The APir is also preferentially targeted by pIC projections,  
421 and reciprocates this connection, which may provide an interesting pathway for odor-related  
422 responses.

423 Accompanying this study we provide an excel sheet that contains the entire dataset (**Suppl.**  
424 **Table 1**). Using the pivot table function of Microsoft Excel allows to recreate any plot presented  
425 in this study and to query and reanalyze the datasets for individual questions. In the excel sheet,  
426 we provide five example pivot tables and describe the workflow to create such tables in **Suppl.**  
427 **Fig. 6**.

428 Taken together, our dataset combined with functional studies suggest that the insula is a hub that  
429 integrates bodily information with memory and emotional content and to guide behavior and  
430 maintain homeostasis.

## 431 **Materials and Methods**

### 432 **Animals**

433 Mice between 2–6 months of age were used in accordance with the regulations from the  
434 government of Upper Bavaria. CamKII $\alpha$ -Cre (B6.Cg-Tg(Camk2a-cre)T29-1Stl/J) mice were  
435 used for both retrograde rabies virus tracings and anterograde axonal tracings. Retrograde rabies  
436 virus tracings were also performed in GAD2-Cre (Gad2tm2(cre)Zjh/J) mice. Both female and  
437 male mice were employed (Fig S1c). For controls, we used male C57Bl6\NRj mice. All mice  
438 group housed 2-4 mice / cage and were kept on an inverted 12 h light/dark cycle (lights off at  
439 11:00 am). Mice were provided with *ad libitum* access to standard chow and water.

### 440 **Viral constructs**

441 Unless otherwise stated, the following constructs were obtained from the UNC Vector Core  
442 (Gene Therapy Center, University of North Carolina at Chapel Hill, USA). For anterograde  
443 tracings AAV2/5-EF1 $\alpha$ -DIO-eYFP ( $5.6 \times 10^{12}$  vg/ml) was used. For retrograde rabies virus  
444 tracings AAV2/8-EF1 $\alpha$ -FLEX-TVA-mCherry ( $4.2 \times 10^{12}$  vg/ml), AAV2/8-CA-FLEX-RG  
445 ( $2.5 \times 10^{12}$  vg/ml), and G-deleted EnvA-pseudotyped rabies virus -eGFP (SAD $\Delta$ G-eGFP(EnvA)  
446 ( $3 \times 10^8$  ffu/ml), were prepared as described before (Gehrlach et al., 2019; Wickersham, Lyon, et  
447 al., 2007).

### 448 **Surgeries**

449 Anesthesia was initiated with 5% isoflurane and maintained at 1-2.5% throughout surgery.  
450 Metamizol (200 mg/kg, s.c., WDT, Garbsen, Germany) was injected for peri-operative analgesia  
451 and carprofen (s.c., 5 mg/kg, once daily for 3 days, Zoetis) for post-operative pain management.  
452 Mice were secured in a stereotaxic frame (Stoelting, IL), placed on a heating pad (37 °C) and eye  
453 ointment (Bepanthen, Bayer) was applied. For viral infusions, pulled glass-pipettes were attached  
454 to a microliter syringe (5  $\mu$ L Model 75 RN, Hamilton, NV) using a glass needle compression  
455 fitting (#55750-01, Hamilton), mounted on a syringe pump controlled by a microcontroller  
456 (UMP3 + micro4, WPI). After trepanation of the skull, mice were unilaterally injected with 100 –  
457 150 nl of a 6:1 (RG: TVA) mixture of helper-viruses. The following coordinates (mm from  
458 Bregma) were used: for anterior IC: AP: +1.9 mm, ML: + or - 2.7 mm, DV: -3.0 mm. For medial  
459 IC: AP: 0.7 mm, ML: + or – 3.7 mm, DV: -4.0 mm. For posterior IC: AP: -0.5 mm, ML: + or –

460 4.05 mm, DV:- 4.0 mm. The trepanation was sealed with bone wax and the skin sutured. After 3-  
461 4 weeks, 350 nl of SADΔG-eGFP(EnvA) was injected into the same coordinates. Mice were  
462 sacrificed 7 days after infusion of the rabies virus. For axonal AAV-tracings in CamKIIα-Cre  
463 mice, AAV2/5-EF1α-DIO-eYFP (80-100 nl) was injected unilaterally into either the aIC, mIC or  
464 pIC coordinates mentioned above. Mice were sacrificed four weeks after the injections.

## 465 **Histology**

466 Animals were anesthetized with ketamine/xylazine (100 mg/kg and 20 mg/kg BW, respectively,  
467 Serumwerk Bernburg) and perfused intra-cardially with 1x PBS followed by 4%  
468 paraformaldehyde (PFA) in PBS. Brains were post-fixed for an additional 24 h in 4% PFA at 4  
469 °C. Brains were embedded in agarose (3% in Water) and 70 μm coronal sections were cut with a  
470 VT1000S vibratome (Leica Biosystems). Every second section, ranging between approximately  
471 +2.65 to -6.2 mm from Bregma, was mounted on glass slides using a custom-made mounting  
472 medium containing Mowiol 4-88 (Roth, Germany) as described elsewhere (“Mowiol mounting  
473 medium,” 2006) with 0.2 mg/mL DAPI (Sigma-Aldrich, MO).

## 474 **Imaging**

475 Slides containing rabies virus tracings were imaged using a 5x/0.15 NA objective on an  
476 Axioplan2 epifluorescent microscope (Zeiss, Jena, Germany) equipped with a Ludl controllable  
477 stage (Visitron Systems, Puchheim, Germany), a CoolSnapHQ<sup>2</sup> CCD camera (Teledyne  
478 Photometrics, AZ), and orchestrated by μManager 2.0 beta software (Edelstein et al., 2014).  
479 Excitation was provided by an X-cite halogen lamp (Excelitas Technologies, MA) with 350/50x  
480 (DAPI) and 470/40x (eGFP) filter cubes.

481 Axonal AAV tracings were imaged on an SP5 or SP8 laser scanning confocal microscope (Leica,  
482 LAS AF and LAS X 3.5.0.18371, respectively) using a 10x/0.40 NA objective, and a 1 Airy disc  
483 pinhole. 405 nm and 488 nm laser lines were used to image DAPI and eYFP channels. Single  
484 optical z-section images of 10 μm thickness from the middle (z-axis) of the section were  
485 acquired. For each brain, we determined the densest efferents outside the insular cortex, and  
486 adjusted the acquisition settings to obtain a nearly saturated signal.

487 Starter volumes for RV tracings were determined by imaging sections covering the injection site  
488 with an SP5 microscope using the 10x objective. 10 z-stacks of 7 μm step-size through each

489 section were acquired. For AAV starter cells, sections covering the injection site were imaged as  
490 a single plane on the epifluorescent microscope with a 5x objective.

#### 491 **Starter volume detection**

492 Both RV and AAV starter cell volumes were determined semi-automatically using CellProfiler  
493 3.0.0 (Kamentsky et al., 2011). For each image, a set of ROIs were defined for the insular and  
494 adjacent regions present. For RV images, rabies virus positive cells were detected in the eGFP  
495 image, and the corresponding cell objects masked over the mCherry (TVA) image. mCherry  
496 signal was then detected and back-related to the eGFP<sup>+</sup> cell. The individual double-positive cells  
497 were traced through the z-stacks and related to their corresponding ROI. For AAV images, eYFP<sup>+</sup>  
498 cells bodies were segmented and related to their corresponding ROI.

#### 499 **Monosynaptic retrograde rabies virus tracing**

500 All image processing was performed in FIJI (Fiji is just ImageJ, NIH). Collated images for each  
501 brain section were stitched to a single image with the Grid/StitchCollection plugin. Autonomous  
502 detection of labelled neurons was performed using a customized macro script. eGFP images were  
503 background subtracted (rolling ball, pixel width 20), and the eGFP<sup>+</sup> cell bodies detected using  
504 Trainable Weka Segmentation (University of Waikato, New Zealand), trained on a small subset  
505 of images for each tracing. Segmented images were binarized and a watershed segmentation run.  
506 To count labelled neurons and assign them to a brain region, a second customized macro script  
507 was used on the binary image. A library of ROIs amalgamated from coronal maps of two mouse  
508 reference atlases (Paxinos and Franklin, and Allen Brain Atlas) was created. For each section, the  
509 corresponding ROI set was adjusted manually to fit the image, and the number of positive cells  
510 determined using the ‘Analyze Particles’ plugin (size =15-1000, circularity=0.10-1.0). Data  
511 output was calculated as cell counts for a given ROI normalized to the total cell counts for the  
512 individual brain (% of total input). Additionally, cell density was calculated as total cell number  
513 per ROI area. The injection site was excluded from the analysis, to ensure no starter cells are  
514 counted as input cells.

## 515 **Axonal AAV tracing**

516 Collated images were stitched for each brain section using Leica Application Suite X  
517 3.3.0.16799. Image processing was done in FIJI using customized macro scripts. First, hessian  
518 ridge detection and thresholding was performed as described elsewhere ([Grider, Chen, & David  
519 Shine, 2006](#)). Briefly, this results in binary images of the eYFP<sup>+</sup> axons while eliminating  
520 background fluorescence. These images were then quantified with a second script where, similar  
521 to the rabies virus quantification, the custom-made ROI atlas was manually adjusted for every  
522 coronal section. Percent of total output was calculated from the thresholded image, with the  
523 eYFP<sup>+</sup> pixel count of each ROI normalized to the total of all eYFP<sup>+</sup> pixels identified from the  
524 individual brain. Additionally, percent innervation density was calculated as the proportion of  
525 eYFP<sup>+</sup> pixels covering the maximal pixel count for its ROI. Clearly distinguishable passing fiber  
526 bundles (such as in the striatum, cerebral peduncles, anterior commissure, internal- and external  
527 capsules, and pyramidal tract) were excluded from the analysis. As with the RV tracings, the  
528 starter volume was also excluded from all analysis.

## 529 **Data collation and statistical analysis**

530 Data was analyzed using a custom-written code in Python 3.6. Cells (for RV) and pixels (for  
531 AAV) were grouped in both 17 large brain regions, and the 75 sub-regions thereof. Regions with  
532 less than 0.03% connectivity were considered below background threshold, and set to zero.

533 To create plots that display the data along the anterior-posterior axis (e.g. % density innervation),  
534 we first linearly interpolated missing values and then smoothed the data using a Savitzky-Golay-  
535 Filter (`scipy.signal.savgol_filter`).

536 For input-output correlations to test for reciprocity, analysis was performed using GraphPad  
537 Prism (GraphPad Software, CA). For the correlation matrices of input vs. input and output vs.  
538 output, the data of the 17 major brain regions (% of total in- or output) was correlated by  
539 computing the pair-wise Pearson's correlation coefficients of all input or output tracings,  
540 respectively. Then, the correlation coefficients were hierarchically clustered with the complete-  
541 linkage clustering method.

542 All animal numbers are reported in Figures and their legends. No statistical methods were used  
543 to predetermine sample size, but it is comparable to published work ([Ährlund-Richter et al.,](#)  
544 [2019; Do et al., 2016; Luo et al., 2019](#)).

## 545 **Acknowledgements**

546 We thank M. Junghänel, F. Lyonnaz, M. Ponsérre for technical assistance and N. Dolensek for in  
547 setting-up the image acquisition pipeline. This study was supported by the Max Planck Society,  
548 the Deutsche Forschungsgemeinschaft (SPP1665 to K.-K.C., D.A.G. and N.G.), funding from  
549 the European Research Council (ERC) under the European Union’s Horizon 2020 research and  
550 innovation programme (ERC-2017-STG, grant agreement 758448 to N.G.), and the ANR-DFG  
551 project ‘SAFENET’ (ANR-17-CE37-0021 to A.K. and N.G.).

## 552 **References**

- 553 Ährlund-Richter, S., Xuan, Y., van Lunteren, J. A., Kim, H., Ortiz, C., Pollak Dorocic, I., ...  
554 Carlén, M. (2019). A whole-brain atlas of monosynaptic input targeting four different cell  
555 types in the medial prefrontal cortex of the mouse. *Nature Neuroscience*, 22(4), 657–668.  
556 <https://doi.org/10.1038/s41593-019-0354-y>
- 557 Allen, G. V., Saper, C. B., Hurley, K. M., & Cechetto, D. F. (1991). Organization of visceral and  
558 limbic connections in the insular cortex of the rat. *The Journal of Comparative Neurology*,  
559 311(1), 1–16. <https://doi.org/10.1002/cne.903110102>
- 560 Augustine, J. R. (1996). Circuitry and functional aspects of the insular lobe in primates including  
561 humans. *Brain Research Reviews*, 22(3), 229–244. [https://doi.org/10.1016/S0165-](https://doi.org/10.1016/S0165-0173(96)00011-2)  
562 [0173\(96\)00011-2](https://doi.org/10.1016/S0165-0173(96)00011-2)
- 563 Beier, K. T., Steinberg, E. E., Deloach, K. E., Xie, S., Miyamichi, K., Schwarz, L., ... Luo, L.  
564 (2015). Circuit Architecture of VTA Dopamine Neurons Revealed by Systematic Input-  
565 Output Mapping. *Cell*, 162(3), 622–634. <https://doi.org/10.1016/j.cell.2015.07.015>
- 566 Bermúdez-Rattoni, F., Okuda, S., Roozendaal, B., & McGaugh, J. L. (2005). Insular cortex is  
567 involved in consolidation of object recognition memory. *Learning & Memory*, 12(5), 447–  
568 449. <https://doi.org/10.1101/lm.97605>
- 569 Brimblecombe, K. R., & Cragg, S. J. (2017, February). The Striosome and Matrix Compartments  
570 of the Striatum: A Path through the Labyrinth from Neurochemistry toward Function. *ACS*  
571 *Chemical Neuroscience*. American Chemical Society.  
572 <https://doi.org/10.1021/acscemneuro.6b00333>
- 573 Cauda, F., Costa, T., Torta, D. M. E., Sacco, K., D’Agata, F., Duca, S., ... Vercelli, A. (2012).  
574 Meta-analytic clustering of the insular cortex. Characterizing the meta-analytic connectivity  
575 of the insula when involved in active tasks. *NeuroImage*, 62(1), 343–355.  
576 <https://doi.org/10.1016/j.neuroimage.2012.04.012>
- 577 Cechetto, D. F., & Saper, C. B. (1987). Evidence for a viscerotopic sensory representation in the

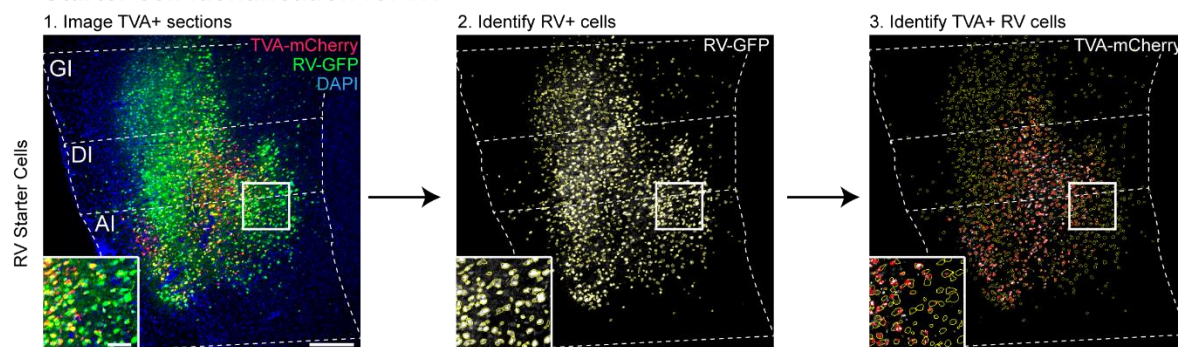
- 578 cortex and thalamus in the rat. *Journal of Comparative Neurology*, 262(1), 27–45.  
579 <https://doi.org/10.1002/cne.902620104>
- 580 Contreras, M., Ceric, F., & Torrealba, F. (2007). Inactivation of the Interoceptive Insula Disrupts  
581 Drug Craving and Malaise Induced by Lithium. *Science*, 318(5850), 655–658.  
582 <https://doi.org/10.1126/science.1145590>
- 583 Craig, A. D B. (2011). Significance of the insula for the evolution of human awareness of  
584 feelings from the body. *Annals of the New York Academy of Sciences*, 1225(1), 72–82.  
585 <https://doi.org/10.1111/j.1749-6632.2011.05990.x>
- 586 Craig, A D Bud. (2009). How do you feel--now? The anterior insula and human awareness.  
587 *Nature Reviews. Neuroscience*, 10(1), 59–70. <https://doi.org/10.1038/nrn2555>
- 588 Crandall, S. R., Cruikshank, S. J., & Connors, B. W. (2015). A Corticothalamic Switch:  
589 Controlling the Thalamus with Dynamic Synapses. *Neuron*, 86(3), 768–782.  
590 <https://doi.org/10.1016/j.neuron.2015.03.040>
- 591 Damasio, A., & Carvalho, G. B. (2013). The nature of feelings: evolutionary and neurobiological  
592 origins. *Nature Reviews. Neuroscience*, 14(2), 143–152. <https://doi.org/10.1038/nrn3403>
- 593 Do, J. P., Xu, M., Lee, S.-H., Chang, W.-C., Zhang, S., Chung, S., ... Dan, Y. (2016). Cell type-  
594 specific long-range connections of basal forebrain circuit. *ELife*, 5.  
595 <https://doi.org/10.7554/eLife.13214>
- 596 Edelstein, A. D., Tsuchida, M. A., Amodaj, N., Pinkard, H., Vale, R. D., & Stuurman, N. (2014).  
597 Advanced methods of microscope control using  $\mu$ Manager software. *Journal of Biological*  
598 *Methods*, 1(2), 10. <https://doi.org/10.14440/jbm.2014.36>
- 599 Etkin, A., Büchel, C., & Gross, J. J. (2015). The neural bases of emotion regulation. *Nature*  
600 *Reviews Neuroscience*, 16(11), 693–700. <https://doi.org/10.1038/nrn4044>
- 601 Fujita, S., Adachi, K., Koshikawa, N., & Kobayashi, M. (2010). Spatiotemporal dynamics of  
602 excitation in rat insular cortex: intrinsic corticocortical circuit regulates caudal-rostro  
603 excitatory propagation from the insular to frontal cortex. *Neuroscience*, 165(1), 278–292.  
604 <https://doi.org/10.1016/j.neuroscience.2009.09.073>
- 605 Gehrlach, D. A., Dolensek, N., Klein, A. S., Roy Chowdhury, R., Matthys, A., Junghänel, M., ...  
606 Gogolla, N. (2019). Aversive state processing in the posterior insular cortex. *Nature*  
607 *Neuroscience*, 22(9), 1424–1437. <https://doi.org/10.1038/s41593-019-0469-1>
- 608 Gogolla, N., Takesian, A. E., Feng, G., Fagiolini, M., & Hensch, T. K. (2014). Sensory  
609 Integration in Mouse Insular Cortex Reflects GABA Circuit Maturation. *Neuron*, 83(4),  
610 894–905. <https://doi.org/10.1016/j.neuron.2014.06.033>
- 611 Graybiel, A. M., & Grafton, S. T. (2015). The striatum: where skills and habits meet. *Cold*  
612 *Spring Harbor Perspectives in Biology*, 7(8), a021691.  
613 <https://doi.org/10.1101/cshperspect.a021691>
- 614 Grider, M. H., Chen, Q., & David Shine, H. (2006). Semi-automated quantification of axonal  
615 densities in labeled CNS tissue. *Journal of Neuroscience Methods*, 155(2), 172–179.  
616 <https://doi.org/10.1016/j.jneumeth.2005.12.021>

- 617 Hintiryan, H., Foster, N. N., Bowman, I., Bay, M., Song, M. Y., Gou, L., ... Dong, H.-W.  
618 (2016). The mouse cortico-striatal projectome. *Nature Neuroscience*, *19*(8), 1100–1114.  
619 <https://doi.org/10.1038/nn.4332>
- 620 Hunnicutt, B. J., Jongbloets, B. C., Birdsong, W. T., Gertz, K. J., Zhong, H., & Mao, T. (2016).  
621 A comprehensive excitatory input map of the striatum reveals novel functional organization.  
622 *ELife*, *5*. <https://doi.org/10.7554/eLife.19103>
- 623 Hunnicutt, B. J., Long, B. R., Kusefoglu, D., Gertz, K. J., Zhong, H., & Mao, T. (2014). A  
624 comprehensive thalamocortical projection map at the mesoscopic level. *Nature*  
625 *Neuroscience*, *17*(9), 1276–1285. <https://doi.org/10.1038/nn.3780>
- 626 Kamentsky, L., Jones, T. R., Fraser, A., Bray, M.-A., Logan, D. J., Madden, K. L., ... Carpenter,  
627 A. E. (2011). Systems biology Improved structure, function and compatibility for  
628 CellProfiler: modular high-throughput image analysis software. *BIOINFORMATICS*  
629 *APPLICATIONS NOTE*, *27*(8), 1179–1180. <https://doi.org/10.1093/bioinformatics/btr095>
- 630 Knowland, D., Lilascharoen, V., Pacia, C. P., Shin, S., Wang, E. H.-J., & Lim, B. K. (2017).  
631 Distinct Ventral Pallidal Neural Populations Mediate Separate Symptoms of Depression.  
632 *Cell*, *170*(2), 284–297.e18. <https://doi.org/10.1016/J.CELL.2017.06.015>
- 633 Kurth, F., Zilles, K., Fox, P. T., Laird, A. R., & Eickhoff, S. B. (2010). A link between the  
634 systems: functional differentiation and integration within the human insula revealed by  
635 meta-analysis. *Brain Structure & Function*, *214*(5–6), 519–534.  
636 <https://doi.org/10.1007/s00429-010-0255-z>
- 637 Lavi, K., Jacobson, G. A., Rosenblum, K., & Lüthi, A. (2018). Encoding of Conditioned Taste  
638 Aversion in Cortico-Amygdala Circuits. *Cell Reports*, *24*(2), 278–283.  
639 <https://doi.org/10.1016/j.celrep.2018.06.053>
- 640 Lein, E. S., Hawrylycz, M. J., Ao, N., Ayres, M., Bensinger, A., Bernard, A., ... Jones, A. R.  
641 (2007). Genome-wide atlas of gene expression in the adult mouse brain. *Nature*, *445*(7124),  
642 168–176. <https://doi.org/10.1038/nature05453>
- 643 Livneh, Y., Ramesh, R. N., Burgess, C. R., Levandowski, K. M., Madara, J. C., Fenselau, H., ...  
644 Andermann, M. L. (2017). Homeostatic circuits selectively gate food cue responses in  
645 insular cortex. *Nature*, *546*(7660), 611–616. <https://doi.org/10.1038/nature22375>
- 646 Livneh, Y., Sugden, A. U., Madara, J. C., Essner, R. A., Flores, V. I., Sugden, L. A., ...  
647 Andermann, M. L. (2020). Estimation of Current and Future Physiological States in Insular  
648 Cortex. *Neuron*. <https://doi.org/10.1016/j.neuron.2019.12.027>
- 649 Luo, P., Li, A., Zheng, Y., Han, Y., Tian, J., Xu, Z., ... Li, X. (2019). Whole Brain Mapping of  
650 Long-Range Direct Input to Glutamatergic and GABAergic Neurons in Motor Cortex.  
651 *Frontiers in Neuroanatomy*, *13*, 44. <https://doi.org/10.3389/fnana.2019.00044>
- 652 Maffei, A., Haley, M., & Fontanini, A. (2012). Neural processing of gustatory information in  
653 insular circuits. *Current Opinion in Neurobiology*, *22*(4), 709–716.  
654 <https://doi.org/10.1016/j.conb.2012.04.001>
- 655 McDonald, A. J., Shammah-Lagnado, S. J., Shi, C., & Davis, M. (1999). Cortical afferents to the  
656 extended amygdala. In *Annals of the New York Academy of Sciences* (Vol. 877, pp. 309–

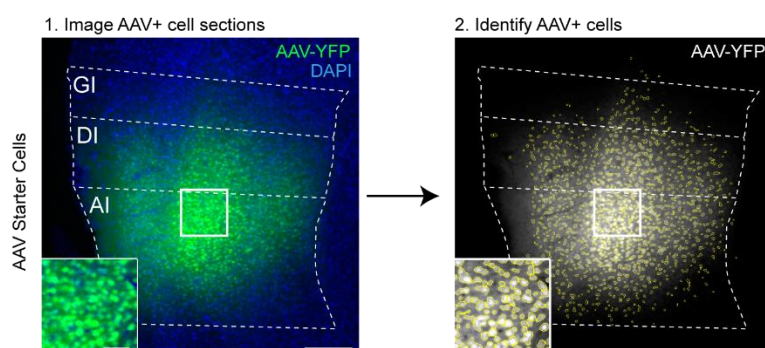
- 657 338). New York Academy of Sciences. <https://doi.org/10.1111/j.1749-6632.1999.tb09275.x>
- 658 Menon, V., & Uddin, L. Q. (2010). Saliency, switching, attention and control: a network model  
659 of insula function. *Brain Structure & Function*, 214(5–6), 655–667.  
660 <https://doi.org/10.1007/s00429-010-0262-0>
- 661 Mowiol mounting medium. (2006). *Cold Spring Harbor Protocols*, 2006(1), pdb.rec10255.  
662 <https://doi.org/10.1101/pdb.rec10255>
- 663 Peng, Y., Gillis-Smith, S., Jin, H., Tränkner, D., Ryba, N. J. P., & Zuker, C. S. (2015). Sweet and  
664 bitter taste in the brain of awake behaving animals. *Nature*, 527(7579), 512–515.  
665 <https://doi.org/10.1038/nature15763>
- 666 Reep, R. L., & Winans, S. S. (1982). Efferent connections of dorsal and ventral agranular insular  
667 cortex in the hamster, *Mesocricetus auratus*. *Neuroscience*, 7(11), 2609–2635.  
668 [https://doi.org/10.1016/0306-4522\(82\)90087-2](https://doi.org/10.1016/0306-4522(82)90087-2)
- 669 Rodgers, K. M., Benison, A. M., Klein, A., & Barth, D. S. (2008). Auditory, somatosensory, and  
670 multisensory insular cortex in the rat. *Cerebral Cortex*, 18(12), 2941–2951.  
671 <https://doi.org/10.1093/cercor/bhn054>
- 672 Rogers-Carter, M. M., Varela, J. A., Gribbons, K. B., Pierce, A. F., McGoey, M. T., Ritchey, M.,  
673 & Christianson, J. P. (2018). Insular cortex mediates approach and avoidance responses to  
674 social affective stimuli. *Nature Neuroscience*. <https://doi.org/10.1038/s41593-018-0071-y>
- 675 Santiago, A. C., & Shammah-Lagnado, S. J. (2005). Afferent connections of the  
676 amygdalopiriform transition area in the rat. *The Journal of Comparative Neurology*, 489(3),  
677 349–371. <https://doi.org/10.1002/cne.20637>
- 678 Schiff, H. C., Bouhuis, A. L., Yu, K., Penzo, M. A., Li, H., He, M., & Li, B. (2018). An Insula-  
679 Central Amygdala Circuit for Guiding Tastant-Reinforced Choice Behavior. *The Journal of*  
680 *Neuroscience: The Official Journal of the Society for Neuroscience*, 38(6), 1418–1429.  
681 <https://doi.org/10.1523/JNEUROSCI.1773-17.2017>
- 682 Sherman, S. M., & Guillery, R. W. (2006). *Exploring the thalamus and its role in cortical*  
683 *function, 2nd ed. Exploring the thalamus and its role in cortical function, 2nd ed.*  
684 Cambridge, MA, US: MIT Press.
- 685 Simmons, W. K., Avery, J. a, Barcalow, J. C., Bodurka, J., Drevets, W. C., & Bellgowan, P.  
686 (2013). Keeping the body in mind: insula functional organization and functional  
687 connectivity integrate interoceptive, exteroceptive, and emotional awareness. *Human Brain*  
688 *Mapping*, 34(11), 2944–2958. <https://doi.org/10.1002/hbm.22113>
- 689 Sohal, V. S., & Rubenstein, J. L. R. (2019). Excitation-inhibition balance as a framework for  
690 investigating mechanisms in neuropsychiatric disorders. *Molecular Psychiatry*, 24(9),  
691 1248–1257. <https://doi.org/10.1038/s41380-019-0426-0>
- 692 Tan, L. L., Pelzer, P., Heigl, C., Tang, W., Gangadharan, V., Flor, H., ... Kuner, R. (2017). A  
693 pathway from midcingulate cortex to posterior insula gates nociceptive hypersensitivity.  
694 *Nature Neuroscience*, 20(11), 1591–1601. <https://doi.org/10.1038/nn.4645>
- 695 Wall, N. R., De La Parra, M., Sorokin, J. M., Taniguchi, H., Huang, Z. J., & Callaway, E. M.  
696 (2016). Brain-Wide Maps of Synaptic Input to Cortical Interneurons. *Journal of*

- 697 *Neuroscience*, 36(14).
- 698 Wall, N. R., Wickersham, I. R., Cetin, A., De La Parra, M., & Callaway, E. M. (2010).  
699 Monosynaptic circuit tracing in vivo through Cre-dependent targeting and complementation  
700 of modified rabies virus. *Proceedings of the National Academy of Sciences of the United*  
701 *States of America*, 107(50), 21848–21853. <https://doi.org/10.1073/pnas.1011756107>
- 702 Wang, L., Gillis-Smith, S., Peng, Y., Zhang, J., Chen, X., Salzman, C. D., ... Zuker, C. S.  
703 (2018). The coding of valence and identity in the mammalian taste system. *Nature*,  
704 558(7708), 127–131. <https://doi.org/10.1038/s41586-018-0165-4>
- 705 Wickersham, I. R., Finke, S., Conzelmann, K.-K., & Callaway, E. M. (2007). Retrograde  
706 neuronal tracing with a deletion-mutant rabies virus. *Nature Methods*, 4(1), 47–49.  
707 <https://doi.org/10.1038/nmeth999>
- 708 Wickersham, I. R., Lyon, D. C., Barnard, R. J. O., Mori, T., Finke, S., Conzelmann, K. K., ...  
709 Callaway, E. M. (2007). Monosynaptic Restriction of Transsynaptic Tracing from Single,  
710 Genetically Targeted Neurons. *Neuron*, 53(5), 639–647.  
711 <https://doi.org/10.1016/j.neuron.2007.01.033>
- 712 Yasui, Y., Breder, C. D., Safer, C. B., & Cechetto, D. F. (1991). Autonomic responses and  
713 efferent pathways from the insular cortex in the rat. *The Journal of Comparative Neurology*,  
714 303(3), 355–374. <https://doi.org/10.1002/cne.903030303>
- 715 Yizhar, O., Fenno, L. E., Prigge, M., Schneider, F., Davidson, T. J., O’Shea, D. J., ... Deisseroth,  
716 K. (2011). Neocortical excitation/inhibition balance in information processing and social  
717 dysfunction. *Nature*, 477(7363), 171–178. <https://doi.org/10.1038/nature10360>
- 718 Zingg, B., Chou, X. lin, Zhang, Z. gang, Mesik, L., Liang, F., Tao, H. W., & Zhang, L. I. (2017).  
719 AAV-Mediated Anterograde Transsynaptic Tagging: Mapping Corticocollicular Input-  
720 Defined Neural Pathways for Defense Behaviors. *Neuron*, 93(1), 33–47.  
721 <https://doi.org/10.1016/j.neuron.2016.11.045>

## a Starter cell identification for RV

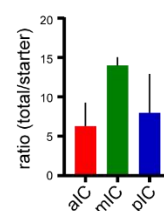


## b Starter cell identification for AAV tracings

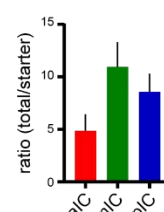


## c Individual mouse data

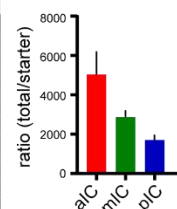
RV CamKII $\alpha$		Starter Cell Location (Bregma)			Starter cell no.	Total input cells	Ratio	Gender	Hemisphere
Target site	Mouse ID	Most anterior	Median	Most posterior					
aIC	872	2.77	1.77	0.8	2278	12197	5.35	female	right
	461	2.4	2.2	1.6	1444	17084	11.83	female	right
	557	2.45	2.09	0.73	15464	27170	1.76	female	left
mIC	1323	1.7	1.21	0.85	3896	46196	11.86	male	right
	460	1.3	0.7	0.2	2921	43618	14.93	female	left
	16	1.2	0.7	0.13	2564	38932	15.18	female	right
pIC	1114	1.25	-0.6	-2.15	2591	10777	4.16	female	right
	175	0.37	-0.11	-1.43	1140	20295	17.80	female	right
	972	0.3	-0.2	-0.7	5379	10561	1.96	female	left



RV Gad2		Starter Cell Location (Bregma)			Starter cell no.	Total input cells	Ratio	Gender	Hemisphere
Target site	Mouse ID	Most anterior	Median	Most posterior					
aIC	1146	2.33	1.93	1.09	1672	6529	3.90	male	right
	1147	2.65	2.2	1.53	1807	14317	7.92	male	right
	1225	2.65	2.2	1.41	1847	5171	2.80	male	right
mIC	1163	1.53	0.13	-0.83	2292	18690	8.15	female	right
	1164	1	0.4	-0.35	1190	10766	9.05	female	right
	1161	1.2	0.25	-0.95	1584	24752	15.63	male	right
pIC	1162	-0.1	-0.8	-1.34	2020	16077	7.96	female	right
	1221	0.13	-0.59	-1.43	912	10791	11.83	female	right
	1224	-0.11	-0.7	-1.2	1027	6021	5.86	female	left



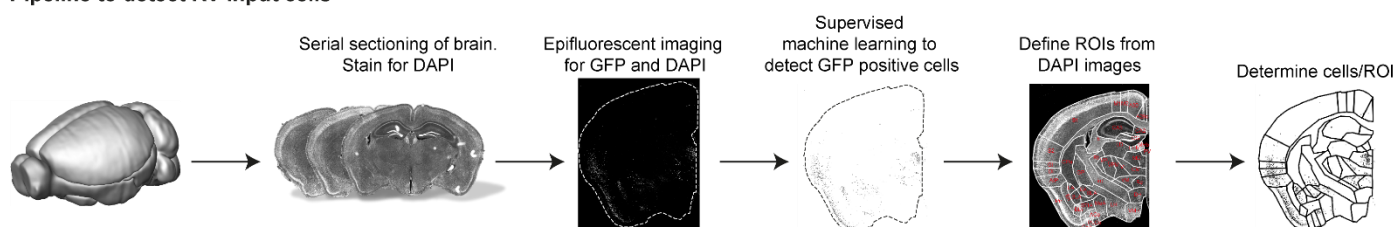
AAV CamKII $\alpha$		Starter Cell Location (Bregma)			Starter cell no.	Total output pixels	Ratio	Gender	Hemisphere
Target site	Mouse ID	Most anterior	Median	Most posterior					
aIC	1294	2.1	1.7	1.2	8464	40730849	4812	female	right
	839	2.65	1.85	1.21	6474	46413601	7169	male	right
	558	2.7	2	1.2	7742	24028624	3104	female	left
mIC	555	1.69	0.85	-0.11	7566	18676912	2469	female	left
	301	1.5	1	0.2	5702	20303273	3561	male	right
	302	1.21	0.61	-0.23	7412	19340592	2609	male	right
pIC	1309	0.85	0.25	-1.23	6830	10610569	1554	female	right
	1310	0.13	-0.44	-1.55	8949	19964251	2231	female	right
	1324	0.25	-0.23	-0.83	4578	6026647	1316	female	right



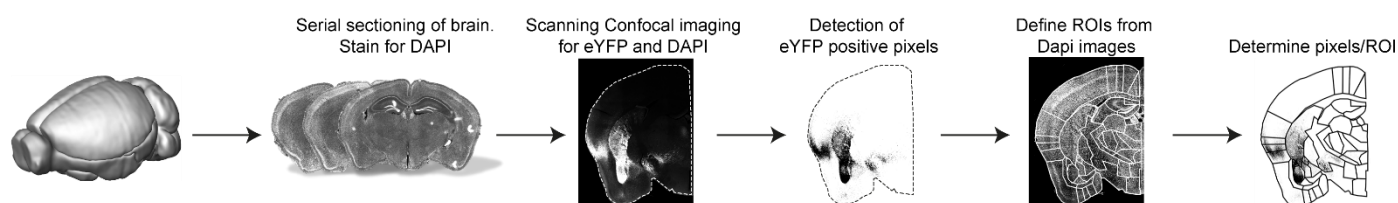
722 **Supplementary Figure 1. Starter cell identification.**

723 **(a)** Starter cell identification pipeline for RV helper system. **1.** High resolution image of a representative  
724 section at the injection site in the IC. Starter cells are double-labelled with TVA-mCherry and RV-GFP, and  
725 appear yellow. Scale bars 200  $\mu\text{m}$  (main image), 50  $\mu\text{m}$  (inset). Number of starter cells were identified in  
726 an automated fashion using Cell Profiler. First RV+ cells were identified (**2.**, yellow cell outlines) from the  
727 GFP image, then RV+ cells that also contain mCherry-TVA were identified from the mCherry signal (**3.**, red  
728 rings within yellow RV+ cell outlines). Double labelled cells were counted as starter cells. **(b)** Starter cell  
729 identification pipeline for AAV tracing system. **1.** Representative epifluorescent image of YFP-labelled AAV  
730 starter cells. Scale bars 200  $\mu\text{m}$  (main image), 50  $\mu\text{m}$  (inset). **2.** YFP-positive cells were identified in an  
731 automated manner using Cell Profiler. Data given as cells per brain subregion, which was manually defined  
732 before cell identification. **(c)** Raw data for each individual animal used. Starter cell range values given as  
733 distance from Bregma in mm. Ratio shown as total cells/starter cells. Hemisphere indicates injection site.

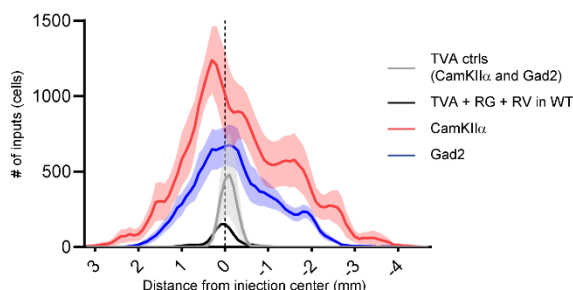
### a Pipeline to detect RV input cells



### b Pipeline to detect AAV output pixels



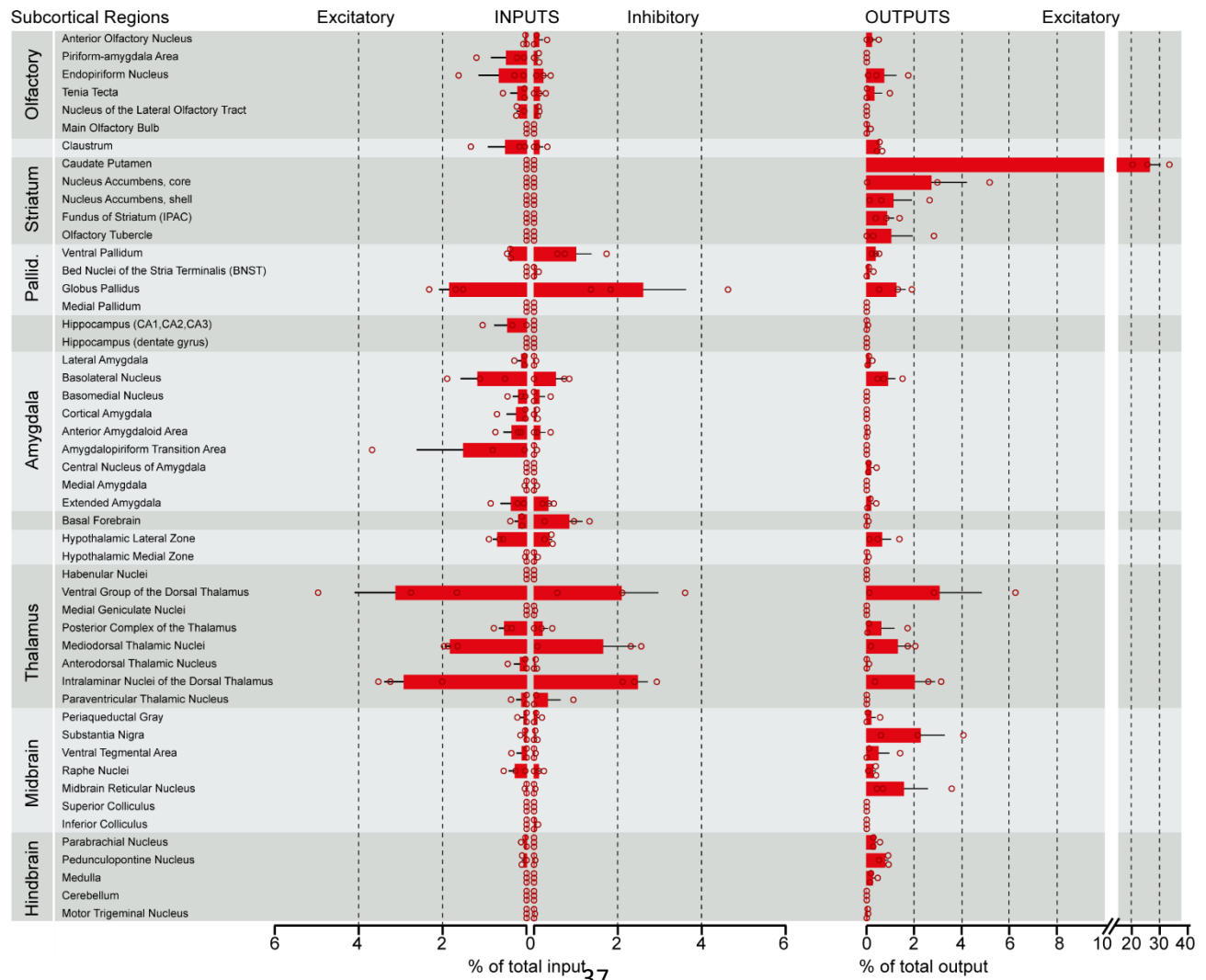
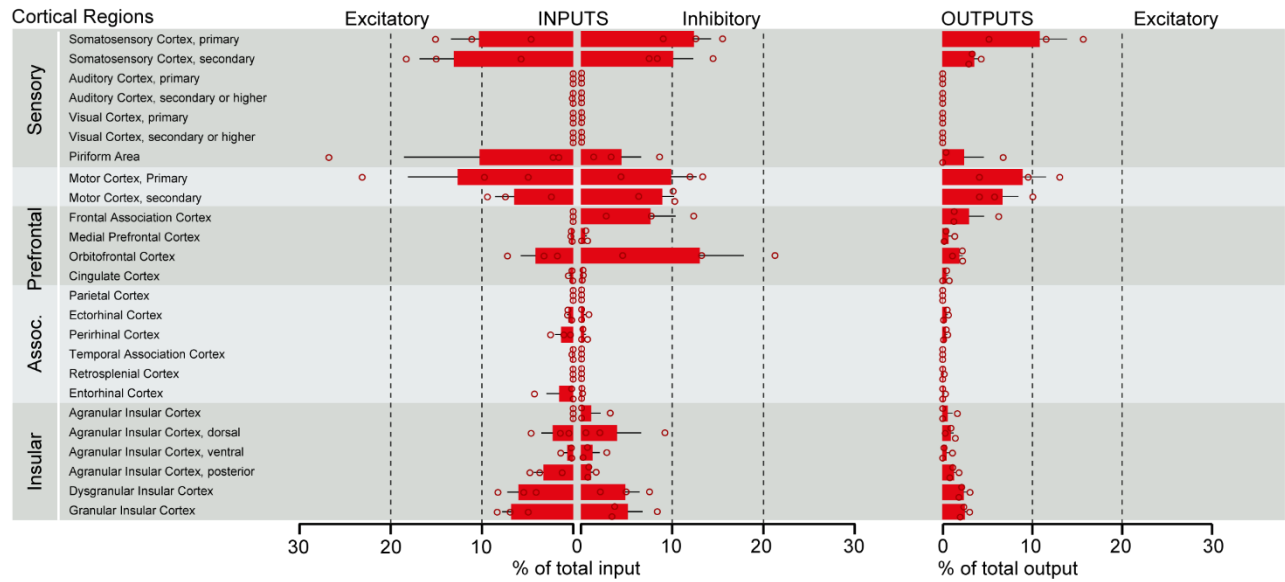
### c Spread of RV+ cells from centre of injection site



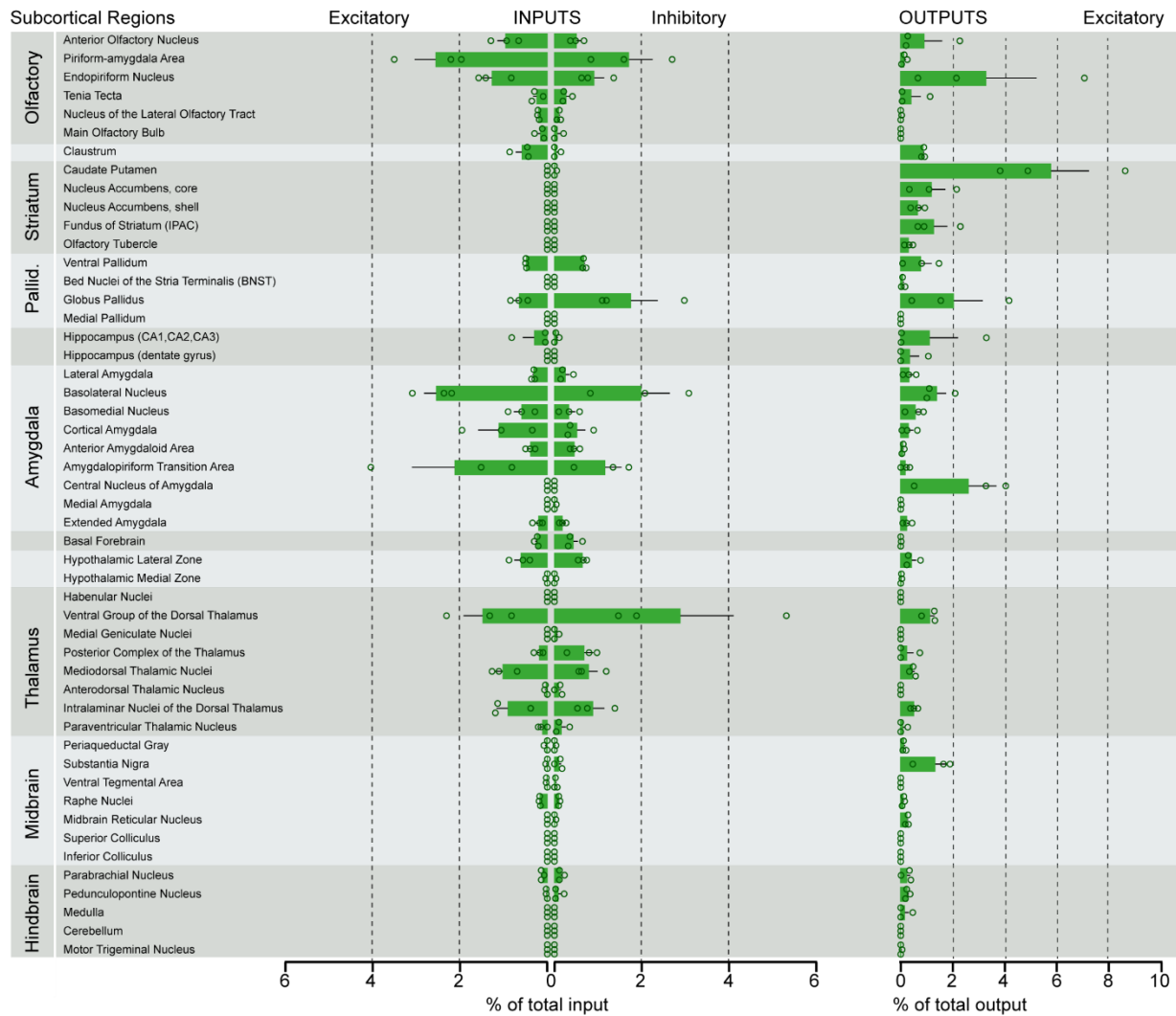
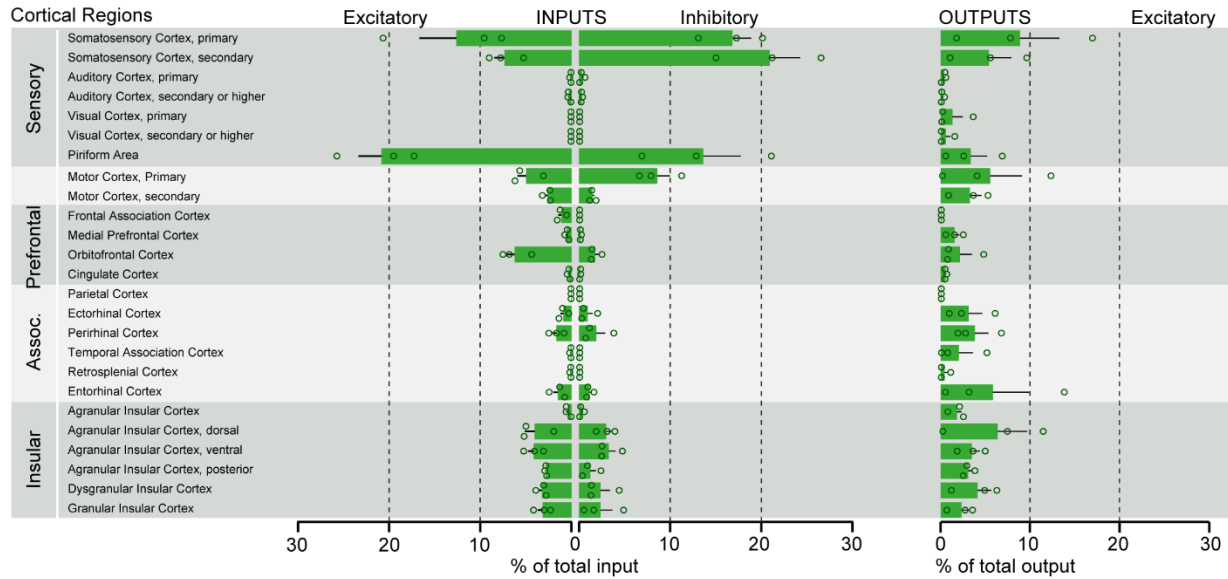
### 734 **Supplementary Figure 2. Tracing pipelines.**

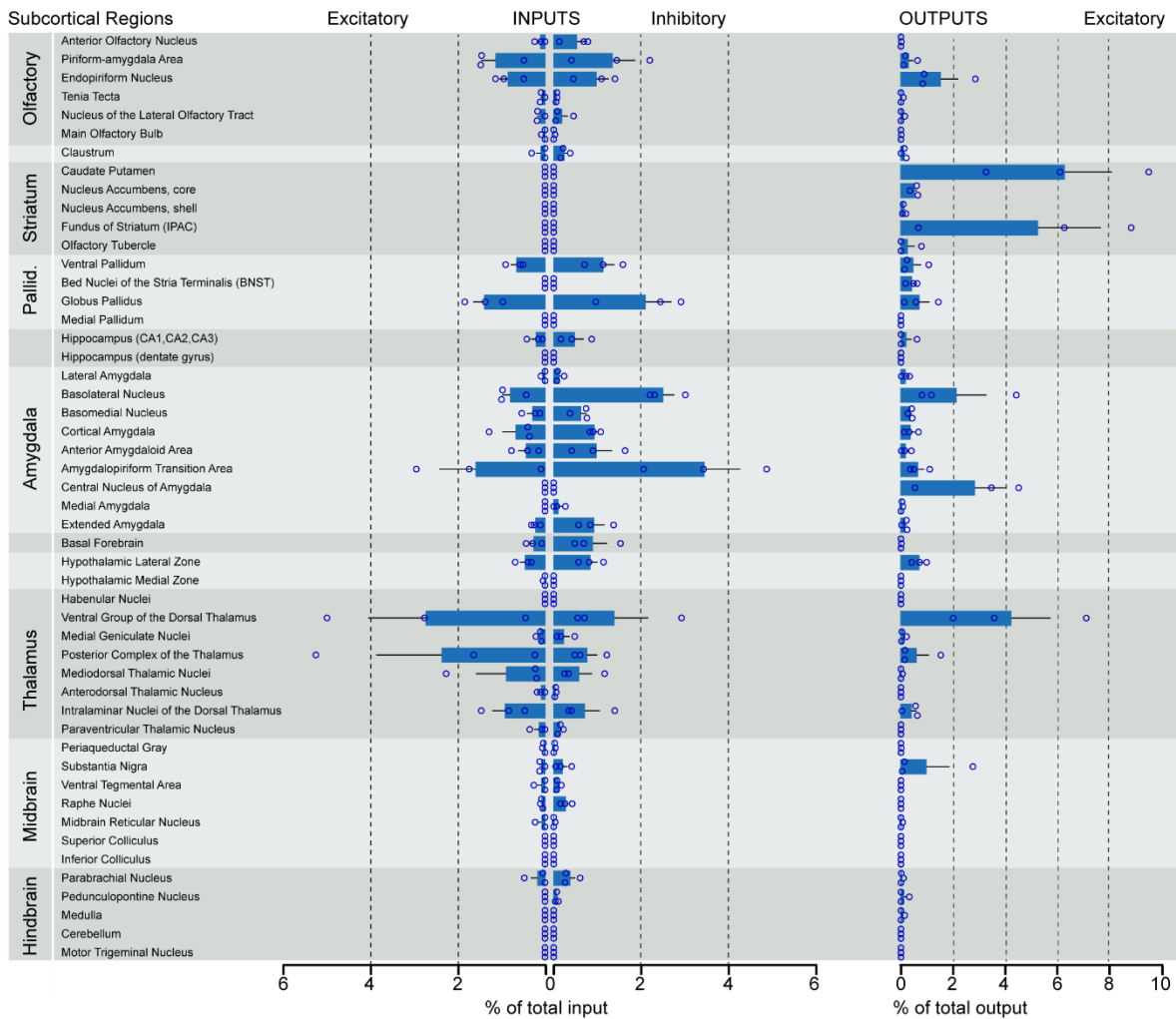
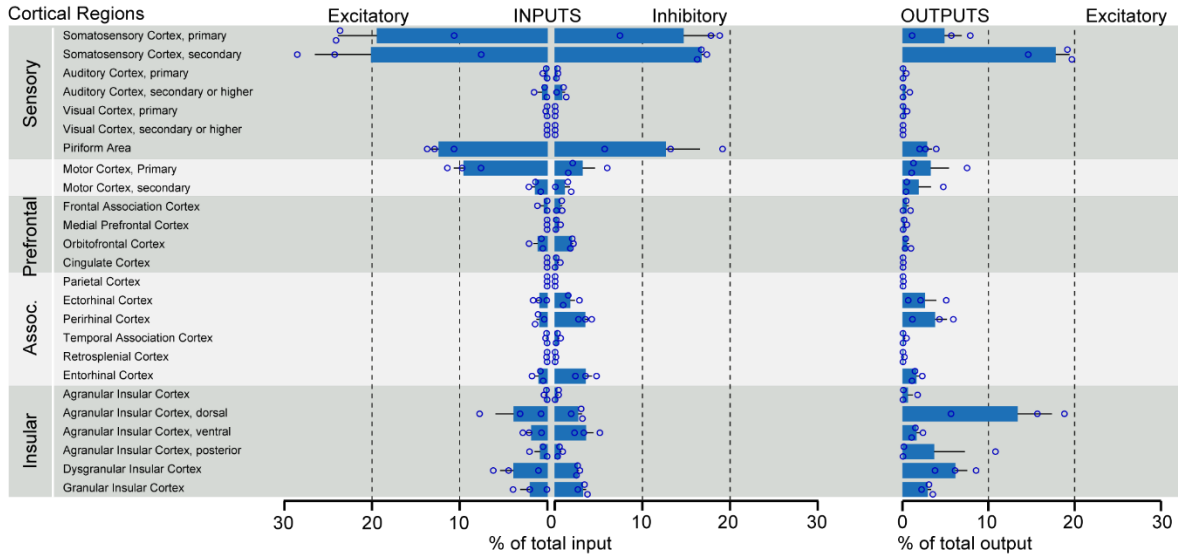
735 Pipeline to detect **(a)** RV+ input neurons to the IC and **(b)** AAV+ output neurons from the IC. Brains were  
 736 fixed and coronally sectioned (thickness: 70  $\mu$ m). Every second section was stained for DAPI and imaged  
 737 either using slide scanner epifluorescent microscopy (RV) or scanning confocal microscopy (AAV). For RV,  
 738 positive cells were identified using supervised machine learning and allocated to manually adjusted ROIs  
 739 corresponding to the Paxinos and Franklin mouse brain atlas. For AAV tracings, YFP positive pixels were  
 740 segmented with hessian ridge detection and allocated to manually adjusted ROIs from the mouse brain  
 741 atlas. **(c)** Assessment of the specificity and spread of experimental and control conditions. In contrast to  
 742 experimental conditions (red: CamKIIa-Cre, N = 9 mice; blue: GAD2-Cre, N = 9 mice), we could not detect  
 743 long-range RV+ neurons in the wildtype- (black, N = 2 mice) and TVA control conditions (grey, N = 2 mice).  
 744 This confirms, that in the experimental conditions, the brain-wide signals are indeed from a transsynaptic  
 745 retrograde transfer. Further, combining the results from the WT controls (black) and TVA controls (grey)  
 746 revealed that there is some leakage of the AAV-FLEX system and that SADdG-eGFP(EnvA) can still infect  
 747 a minor fraction of TVA-negative neurons. Guided by these control experiments, we omitted quantification  
 748 of RV+ neurons for  $\pm$  1mm from the injection center within the IC and claustrum.

aIC



mLC





749 **Supplementary Figure 3-5. Brain-wide datasets for aIC, mIC and pIC.**

750 Brain-wide global datasets were divided into 75 subregions for comparison. Data shows excitatory  
751 (*CamkII $\alpha$* ) and inhibitory (*GAD2*) input strengths, and excitatory output strength (*CamkII $\alpha$* ) from each IC-  
752 subdivision (aIC, mIC, and pIC, Supplementary Figure 3, 4, and 5, respectively). Values are presented as  
753 normalized percentage of total cells (RV) or total pixels (AAV). Data shown as average  $\pm$  SEM. N = 3 mice  
754 per condition. Top panel shows cortical connectivity, bottom panel shows subcortical connectivity.

## How to use the resource excel sheet

1. Select the 'RAW DATA' tab and click on >> **Insert** >> **Pivot Table**, then click 'OK'

2.

### Set Filters

- Tracing\_Type
- Genotype
- Tracing\_From
- (- Large Brain Regions)

PivotTable Fields

Choose fields to add to report: [Settings]

Search

- Index
- Tracing\_Type
- Genotype
- Tracing\_From
- Animal
- Injection Center
- Subregions
- Larger Brain Regions
- Bregma
- Count [Cells or Pixels]
- Area [ $\mu\text{m}^2$ ]
- Pixel Density [Pixel/ $\text{mm}^2$ ]
- Percent\_Total\_Output
- Percent\_Density\_Output
- Cell\_Density[cells/ $\text{mm}^2$ ]<sub>Input</sub>
- Percent\_Total\_Input

MORE TABLES...

Drag fields between areas below:

FILTERS	COLUMNS
Tracing_Type	Animal
Genotype	
Tracing_From	
Larger Brain Regions	

ROWS	VALUES
Subregions	Sum of Percent_Tot...

Defer Layout Update UPDATE

3.

### Choose Values

- % of total input
- % of total output
- Pixel Density
- Cell Density

4.

In the 'Value Field Settings' use "sum of .." for "Percent Total Input/Output" or use "average of" for "Pixel/Cell Density"

5.

Select the pivot table and insert chart

755 **Supplementary Figure 6. Instructions to query the datasets with custom questions.**

756 From the accompanying excel resource sheet, all plots presented in this study can be recreated. In addition,  
757 the reader can query the dataset with his own questions, by creating pivot tables. The workflow, how to  
758 create such a pivot table in excel is described here. **1.** After opening the excel sheet, navigate to the 'RAW  
759 DATA' tab. Then go to the 'Insert' tab and insert a Pivot Table. In the subsequent pop-up dialogue, make  
760 sure the entire range of the dataset is selected and click 'OK'. Next, **2.** set Filters for at least the tracing  
761 type (AAV or RV), as RV and AAV results do not share the same values. Optionally, you can set filters for  
762 the Genotype (CamKIIa and GAD2) and from which part of the insula the tracings should be selected (aIC,  
763 mIC, pIC). Depending on your question and how you want the data to be plotted, you have to choose which  
764 values to use (**3.**). In the manuscript we present the data as percent of total output or input, respectively.  
765 Additionally, we provide cell density and pixel density measurements for RV and AAV tracings, respectively.  
766 **Important: 4.** Because of the raw data structure, it is necessary to use "sum of percent\_total\_input or  
767 output". Double-check that the percentages add up to 100% in the grand total fields. For density  
768 measurements, please use "average of". **5.** Depending on how you want the data to be arranged, drag and  
769 drop the fields into either columns or rows window. E.g. if you are interested in inputs from a region along  
770 the anterior-posterior axis, put "Bregma" into either Columns or Rows. Then select the entire pivot table  
771 and insert a chart.

Low Hierarchy	Abbreviation   name					
	level 1		level 2		level 3	
Amygdala	AA	anterior amygdaloid area				
	APir	amygdalopiriform transition area				
	BLA	basolateral amygdaloid nucleus	aBLA	anterior part		
			pBLA	posterior part		
			vBLA	ventral part		
	BMA	basomedial amygdaloid nucleus	aBMA	anterior part		
			pBMA	posterior part		
	CeA	central nucleus of the amygdala	CeC	capsular part		
			CeL	lateral part		
			CeM	medial part		
LA	lateral amygdala					
EA	extended amygdala					
MeA	medial amygdaloid nucleus					
ACo	cortical amygdala areas					
Assoc. Cortex	ECT	ectothalamic cortex				
	ENT	entorhinal cortex				
	RSP	retrosplenial cortex				
	TeA	temporal association cortex				
	PERI	perirhinal cortex				
	PtA	parietal association cortex				
Basal Forebrain	BF	basal forebrain				
Clastrum	Cl	claustrum				
Hindbrain	PBN	parabrachial nucleus				
	PPN	pedunculopontine nucleus				
	MY	medulla				
	CB	cerebellum				
	V	motor trigeminal nucleus				
Hippocampus	CA1, CA2, CA3	hippocampus (CA1, CA2, CA3)				
	DG	hippocampus (Dentate gyrus)				
Hypothalamus	LHZ	hypothalamus, lateral zone				
	MHZ	hypothalamus, medial zone				
Insular Cortex	AI	agranular insular cortex	AID	dorsal part		
			AIV	ventral part		
			AIP	posterior part		
	DI	dysgranular insular cortex				
Midbrain	SNr	substantia nigra				
Motor Cortex	M1	primary motor cortex				
	M2	secondary motor cortex				
Olfactory	AON	anterior olfactory nucleus				
	CxA	piriform-amygdala area				
	En	endopiriform nucleus				
	TT	tenia tecta				
	LOT	nucleus of the lateral olfactory tract				
	MOB	main olfactory bulb				
Pallidum	BNST	bed nuclei of the stria terminus				
	GP	globus pallidus				
	PALv	ventral pallidum				
	PALm	medial pallidum				
Piriform	Pir	piriform cortex				
Prefrontal	CG	cingulate cortex				
	mPFC	medial prefrontal cortex				
Sensory	OFC	orbitofrontal cortex				
	S1	primary somatosensory cortex				
	S2	secondary somatosensory cortex				
	Au1	primary auditory cortex				
	Au2	secondary auditory cortex				
	V1	primary visual cortex				
Striatum	V2	secondary visual cortex, or higher				
	CPu	caudate putamen				
	NACc	nucleus accumbens, core				
	NACsh	nucleus accumbens, shell				
	IPAC	interstitial nucleus of the posterior limb of the anterior commissure				
Thalamus	Tu	olfactory tubercle				
	VENT	ventral group of the dorsal thalamus	VAL	ventral anterior-lateral nucleus		
			VM	ventral medial nucleus		
			VP	ventral posterior complex	VPL	ventral posterolateral complex
	MGN	medial geniculate nucleus			VPLpc	ventral posterolateral complex, parvicellular part
					VPM	ventral posteromedial nucleus
					VPMpc	ventral posteromedial nucleus, parvicellular part
	ILM	intralaminar nuclei	RH	rhomboid nucleus		
			CM	central medial nucleus		
PaF			parafascicular nucleus			
Hb	habenular nuclei					

772 **Supplementary Table 2. List of abbreviations of larger brain regions and their subdivisions.**